CAN COMPTON SCATTER IMAGING BE INCORPORATED WITH THE MICRO-X CT SCANNER PROTOTYPE TO AID IN THE DETECTION OF STROKE?

By

Erica Nunn

Academic Supervisor: Associate Professor Egon Perilli

Industry Supervisor: Chris Delnooz

Thesis
Submitted to Flinders University
for the degree of

Bachelor of Engineering (Biomedical) (Honours) / Master of Engineering (Biomedical)

College of Science and Engineering

Table of Contents

List of Tables

List of Equations

Abstract

Micro-X is developing a computed tomography (CT) scanner for the detection of stroke in ambulances to assist in the global recognised need for earlier detection and treatment of strokes. Whilst often thought to be an unwanted component in radiological imaging, Compton scattered radiation can provide helpful information as the process is dependent on the scattering medium. To add a secondary image contrast to aid in the detection of stroke, this study will investigate how the scatter produced during the CT scan can be used to the diagnostic team's advantage through the implementation of Compton Scatter Imaging (CSI). To complete a thorough investigation, a literature review of the current CSI technology and stroke pathophysiology was conducted. Differential scatter cross-sections were then calculated to hypothesise what the Compton scatter signal would be. CSI data was then modelled through Monte Carlo simulations performed using the GEANT4 toolkit and statistical data analysis was conducted. The mean and standard deviations of the region of interest selected in the output images of the Monte Carlo simulations was calculated. It was found that using traditional X-ray systems, the difference in photon intensities at the detector is not significantly different for ischemia and healthy tissue at 0.11% (P = 0.7428). Comparatively, the difference between ischemic and healthy tissue in the Compton scatter imaging system was found to be statistically significant at 2.06% (P=0.0007). It was concluded that this preliminary research showed promising results that CSI could be incorporated with the Micro-X CT scanner.

Declaration

I certify that this thesis:

1. does not incorporate without acknowledgment any material previously submitted for a degree or diploma in any university

2. and the research within will not be submitted for any other future degree or diploma without the permission of Flinders University; and

3. to the best of my knowledge and belief, does not contain any material previously published or written by another person except where due reference is made in the text.

Signature of student..

Print name of student: Erica Nunn

Date 12/10/2022 ....

I certify that I have read this thesis. In my opinion it is/is not (please circle) fully adequate, in scope and in quality, as a thesis for the degree of Bachelor of Engineering (Biomedical) (Honours) / Master of Engineering (Biomedical). Furthermore, I confirm that I have provided feedback on this thesis and the student has implemented it minimally/partially/fully (please circle).

Signature of Principal Supervisor..

Print name of Principal Supervisor: Egon Perilli

Date 12/10/2022 ....

Acknowledgements

I would like to acknowledge and express my sincere gratitude to my academic supervisor, Associate Professor Egon Perilli of Flinders University for his assistance and support at every stage of my Masters project. I am deeply grateful for his insightful comments and suggestions.

I would also like to acknowledge and thank the team at Micro-X for not only giving me the opportunity to complete this Masters project, but for their support throughout this project and the last two years of my degree. I want to extend my thanks to Brian Gonzales, for his medical physics and imaging knowledge and support, and my supervisors Chris Delnooz and Anthony Skeats for their unwavering support and belief in me.

Chapter 1: Introduction

Stroke accounts for 25% of Australian deaths, and is the leading cause of disability (AIHW, 2021). Strokes can be classified into two different types; ischemic where a blood clot stops the flow of blow and hemorrhagic where a blood vessel burst and blood pools within the brain (Hui, Tadi and Patti, 2021). If early analysis and treatment can be provided, more than 80% of stroke deaths and related disabilities can be prevented. Nonetheless, any stroke treatment method first requires a medical diagnosis enabled by imaging, typically via Computed Tomography (CT) or Magnetic Resonance Imaging (MRI) (Musuka *et al.*, 2015). The main goal of stroke imaging is to identify the nature of the stroke so the appropriate treatment can be administered (Kurz *et al.*, 2016).

Micro-X is developing a Computed Tomography (CT) Scanner Prototype (figure 1) for the detection of stroke in Ambulances. The prototype models a solid-state CT device consisting of stationary cold-cathode X-ray tubes, as envisioned by Micro-X. The prototype is a dual energy CT scanner with a novel geometry and a curved detector. The prototype is being developed based on the recognised global need for earlier detection of stroke.

Figure removed due to copyright restriction.

Figure 1: Micro-X CT Scanner, Image supplied by Micro-X

Short scanning time, the reduction of motion artefact and the product's light weight and portability are just some of the intended advantages of the Micro-X CT Scanner Prototype compared with traditional CT technology. A number of limitations, however, have been identified such as image artefacts due to its limited angle during scanning and the scattering of X-rays as they interact with matter, which impacts the Micro-X CT Scanner Prototype's ability to detect strokes. Furthermore, the current prototype detects strokes via identifying

haemorrhagic strokes. Medical practitioners have identified a desire for ischemic stroke imaging. Traditional clinical settings use CT perfusion (CTP) imaging to achieve this (Lin and Liebeskind, 2016). CTP requires an intravenous contrast agent, exposes the patient to an extra, longer CT scan with extra radiation and is extremely susceptible to motion artefact (Campbell *et al.*, 2013; Demeestere *et al.*, 2020).

Whilst often thought to be an unwanted component in radiological imaging, scattered radiation can provide helpful information as the process is dependent on the scattering medium. To add a secondary image contrast to aid in the detection of stroke and appease medical practitioners' desires for ischemic imaging, this study will investigate how the scatter produced during the CT scan can be used to the diagnostic team's advantage. The viability of Compton Scatter Imaging (CSI) will be investigated. CSI utilises one of the dominant X-ray interactions with matter, Compton Scatter.

Presently, clinical CTs have used CSI to distinguish between healthy and diseased soft tissue in the breast (Ryan, Farquharson and Flinton, 2005). The implementation of CSI to aid in the detection of stroke has yet to be performed with clinical CT. As the intention is to use the Micro-X CT Scanner Prototype for detecting stroke, this study explores the viability of using CSI to enable this. Due to the limited availability to obtain appropriate physical X-ray detectors and delays in acquiring materials, this study will explore the viability through the use of Monte Carlo simulations.

Chapter 2: Literature Review

2.1 Stroke

Strokes have a lasting impact on the community as they are one of the largest causes of adult disability, with physical consequences including, but not limited to, paralysis, motor function deficits and cognitive impairments (Queensland Brain Institue, 2020). In 2020 alone, more than 27,000 Australians had a stroke. Stroke is one of the leading causes of death globally with an estimate of 4.5 million deaths a year. It is further estimated that by 2050 the rate of incidence of stroke will increase from one every 19 minutes to every 10 (Wolfe, 2000).

Stroke is a medical emergency where interruption to the brain's blood supply causes damage to the brain. There are two types of strokes. Ischemic strokes account for 85% of all strokes and occur when a blood clot or plaque blocks the blood vessel, disrupting the blood supply. When an artery breaks or bursts causing a bleed on the brain, the stroke is known as a hemorrhagic stroke. These two types of strokes have vastly differing treatments. A "clot busting" injection of tissue plasminogen activator (tPA) is considered the first line of treatment for ischemic strokes. If tPA is administered to a patient with a hemorrhagic stroke, it would increase the bleeding which can lead to death. CT stroke imaging is critical in acute stroke care decision making. The Organisation for Economic Co-operation and Development's (OECD) investigation of stroke care in the developed world found all 17 countries included in the study used CT imaging as part of their acute stroke care protocol, as it helps clinicians differentiate ischemia from hemorrhage, excludes stroke mimics such as transient ischemic attacks (TIA) and tumours (Kamalian and Lev 2019; Molina and Saver 2005; Powers et al. 2019). Clinicians also use other imaging modalities such as CTP to determine volume of irreversible infarcted brain tissue, assess the status of large cervical and intracranial arteries and estimate the extent of possibly salvageable brain tissue at risk.

During a stroke, time is an extremely critical factor regarding stroke outcomes. Brain cells in a stroke die at a rate of 1.9 million a minute. For ischemic strokes, if tPA can be administered within the first 4.5 hours of the stroke onset, the patient's chance of recovering drastically increases and fewer complications are reported (Friedman, 1996; Broderick, 1997; Kwiatkowski *et al.*, 1999). Furthermore, several studies comparing tPA with other standard acute ischemic stroke treatments endorses tPA's effectiveness in decreasing mortality and disabilities in stroke patients (Grotta, 2014). Moreover, the National Institute of Neurological

Disorders and Stroke (NINDS) studies suggest that the number of patients who receive tPA treatment will recover without a significant disability is close to 50% ('Tissue plasminogen activator for acute ischemic stroke', 1995). Whilst tPA improves outcomes, it is estimated only 2-12% of ischemic stroke patients receive the treatment (Fassbender *et al.*, 2013; Haass *et al.*, 2014). One of the biggest factors in the dismal treatment numbers and underutilization of tPA is attributed to most patients arriving at hospitals far too late for treatment (Fassbender *et al.*, 2013). A particular CT scanner currently being developed by Micro-X's is the proposed solution to ensure stroke patients receive faster stroke imaging and treatment.

2.2 Compton Scatter Imaging (CSI)

CSI is a radiological imaging technique where the detection of Compton scattered X-rays form the image. Compton scattering occurs during the interaction of high energy photons (30keV to 30MeV) with charged particles (Ziessman, O'Malley and Thrall, 2006). Compton scatter is the dominant interaction with human tissue for the diagnostic X-ray energy range, 30keV to 100keV (Bushberg & Leidholdt, 2002). Unlike traditional X-ray systems, in CSI, the image intensity is proportional to the electron density of the scattering medium, whereas traditional systems the intensity is inversely proportional to the density of the attenuating medium (Yan, Tian and Shao, 2018). This means two materials with the same densities but different molecular makeups would have the same image intensity on traditional X-ray systems output images but different image intensities on Compton scatter output images.
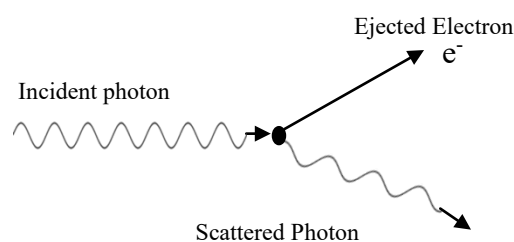
Figure 2: diagram of the Compton scattering process. In regard to Compton Scattering in diagnostic X-rays, the X-ray photon is scattered with reduced energy after ejecting an electron from the atom's outer shell.

Comparing CSI with traditional X-ray techniques, traditional X-ray systems have the sample in-between the detector and source whereas the detector in CSI is offset and often on the same side of the sample as the source.
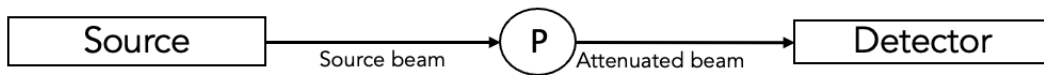
Figure 3a
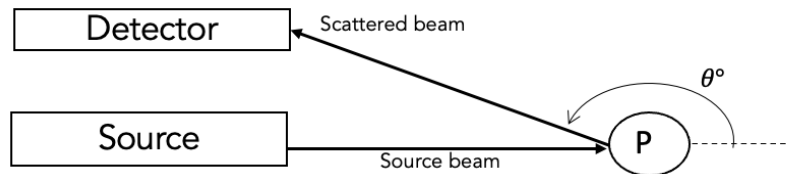
Figure 3b

Figure 3: 3a: Traditional X-ray system schematic. The sample being investigated is situated in-between the source and detector. The detector detects the attenuated source beam. 3b: CSI System Schematic. The detector is positioned offset compared with the traditional system. This setup allows for the scattered beam to be detected rather than the attenuated source beam.

D = detector, S = Source, P = Patient, Images drawn by Erica Nunn

2.2.1 History

In 1959 CSI was introduced to the medical field when Lale, 1959, first used CSI to examine internal organs during radiotherapy (Lale, 1959). Following Lale's work, CSI was widely utilised in medical research in 1979 for bone densitometry (Huddleston, Bhaduri and Weaver, 1979), lung function testing (Kaufman *et al.*, 1976; Garnett *et al.*, 1977; Del Guerra *et al.*, 1982), and heart motion in 1994 (Herr *et al.*, 1994). With the advancement of CT in the late 1970s, the research into CSI in the medical field slowly diminished. CSI subsequently was utilised outside the medical field and applied to non-destructive testing. Most notably CSI has been used in security imaging for drug and explosive imaging and non-destructive testing of large homogenous materials such as soil and concrete (Harding and Harding, 2010).

2.2.2 Current Technology and Developments

CSI is now an established imaging technique used for material differentiation outside of medical settings. Due to the rise and advancement of CSI in non-destructive imaging, further research into CSI's applications in medicine have resumed. Initially, in 1998 Al-Bahri and Spyrou implemented the use of CSI for breast tissue characterisation through mapping the

electron densities. Al-Bahri and Spyrou could map the electron density differences, using CSI, of tumours adipose and glandular tissues with a 3% difference between the tissues (see table 1). Unfortunately, the error margin, of 5%, of Al-Bahri and Spyrou's results was larger than the differences in the electron densities, subsequently adding ambiguity to the study outcomes. Ryan, Farquharson and Flinton in 2005 used CSI like Al-Bahri and Spyrou however choose to offset the detector at 30 degrees compared to Al-Bahri and Spyrou's 90 degrees. Other changes in the methods used included Ryan *et al.* using a tungsten X-ray tube as the source compared with Al-Bahri's use of Americium. The mean electron densities mapped by Ryan, Farquharson and Flinton all fell within the range of Al-Bahri and Spyrou's results, supporting Al-Bahri and Spyrou's results (see table 1). Ryan *et al.*'s significantly lower error margin compared with Al-Bahri *et al.*'s study aids to the confidence of the results. Ryan and Farquharson completed further study in 2007 to create a multivariant analysis tool for their breast tissue classification. Part of this study required the team to use CSI for the characterisation of different tissues in the breast like Al-Bahri *et al.* and Ryan *et al.*'s previous study in 2005. The results of this study in 2007 (see table 1) yield similar mean electron density results compared with the study in 2005 and Al-Bahri and Spyrou's study however Ryan and Farquharson stated in their results section that the experimental setup was not optimised resulting in high statistical errors compared with the other studies.

CSI has also been used to image lung tissues during imaging studies. Jones *et al.* in 2018 used CSI to from scatter intensity maps of patient lungs, rather than electron density maps like Al-Bahri *et al.* and Ryan *et al.*, to characterise the 4 tissues in the lung studies; bone, water, healthy lung tissue and tumour. At the same time, Redler *et al.* in 2018 also found that CSI is a promising modality for directly imaging a patient without the need for extra radiation. Whilst Jones *et al.* were using physical phantoms and radiation, Redler *et al.* utilised Monte Carlo simulations. Similar to Al-Bhari *et al.*, Redler *et al.* and Jones *et al.* had the detector placed at a 90-degree offset. Both Jones *et al.* and Redler *et al.* stated that CSI has the ability to complement existing imaging technologies. The results of these 5 studies are summarised in the table 1 below.

Table 1: Summary of CSI tissue characterisation studies techniques and results. detector location refers to θ° in figure 3b.

Study Details			Technique			Results	
Body Part	**Study**	**Tissues**	**Number of Samples**	**X-ray Source**	**Detector Location**	**Electron Density Maps**	**Scatter Intensity Maps**
Breast	Al-Bahri and Spyrou (1998)	Tumour Adipose Glandular	T = 9 A = 9 G = 9	Americium-241 typical photon output 59.5keV	90°	T = 3.65±0.46 A = 3.47±0.53 G = 3.74±0.61	N/A
	Ryan et al (2005)	Fibroadenoma (FA) Fibrocystic Change (FCC) Malignancy Adipose	FA = 10 FCC= 8 M = 16 A=10	Tungsten industrial X-ray tube 57.97keV	30°	FA =3.31±0.14 FCC =3.65±0.15 M =3.53±0.15 A =3.24±0.14	N/A
	Ryan et al (2007)	Fibroadenoma (FA) Normal Fibrocystic Change (FCC) Malignancy Adipose	FA = 5 N = 8 FCC = 4 M = 12 A = 10	Tungsten industrial X-ray tube 57.97keV	30°	FA =3.31±0.07 N =3.34±0.19 FCC =3.58±0.25 M =3.51±0.19 A =3.25±0.12	N/A
Lung	Jones (2018)	Bone Water Lung Tumour	B=10 W=10 L=10 T=10	6 MV flattening-filter-free therapy beam 140keV-220keV	90°	N/A	B =1.25±0.10 W =1.00±0.04 L =0.28±0.08 T =0.58±0.12
	Redler (2018)	Bone Water Lung Tumour	B=3 W=3 L=3 T=3	Source beam from X-ray tube with 140 kVp	90°	N/A	B =1.30±0.08 W =1.00±0.08 L =0.30±0.02 T =0.57±0.04

2.2.3 Advantages of CSI

A number of attractive features of CSI have been deduced whilst reviewing a number of CSI studies. CSI as an imaging modality used on its own has advantages of source and detector location flexibility compared with traditional X-ray projection techniques (Redler *et al.*, 2018), allowing for unique and novel imaging geometries specific to the CSI use. Other advantages include a greater sensitivity to density variations in low density materials compared to transmission mode X-ray systems (Ryan and Farquharson, 2007; Yan, Tian and Shao, 2018). Advantages of pairing CSI as a secondary imaging mechanism with an existing system includes not only obtaining a secondary image contrast, but the acquisition phase requires no extra radiation exposure to the patient. Furthermore, shielding requirements for the primary system can be reduced as the extra detectors can be used as secondary radiation barriers (Yang *et al.*, 2020).

2.2.4 Limitations of CSI

Whilst CSI has a number of attractive features, there are also a number of limitations presented in the current CSI research. Firstly, very minimal studies of CSI have successfully transitioned from research into commercialised devices used in the medical world. While CSI is commercially used for security and non-destructive imaging, no CSI devices are used clinically. Furthermore, in contrast to traditional X-ray systems, CSI systems require a number of correction algorithms to reduce the impact of multiple scattering and primary beam attenuation(Jones *et al.*, 2018; Redler *et al.*, 2018).

2.3 Monte Carlo Simulations

In building, developing and testing of radiological systems, simulations play a vital role in economically analysing and predicting the performance of new systems (Zou *et al.*, 2010). Simulations allow for numerous tests once built and can be used efficiently to optimise the CT system without the need to invest large sums of money into physical hardware (Hirayama and Hirayama, 2000; Kippen, 2004; Zou *et al.*, 2010). Generally, X-ray systems have 2 common simulation methods, analytical and statistical. Whilst analytical methods have shorter computational times, statistical methods in the form of Monte Carlo simulations have become the industry simulation standard for its ability to accurately reflect particle interaction physics (Agostinelli *et al.*, 2003; Zou *et al.*, 2010; Yang *et al.*, 2020).

Monte Carlo simulations are simulations which take advantage of the Monte Carlo Method. The Monte Carlo Method is a broad class of computational algorithms that solve and model problems using repeated randomness. They solve problems that might be deterministic in principle and relies on randomness to do so (Harrison, 2010). There are numerous open-source Monte Carlo simulation toolkits which are capable of simulating and tracking nuclear particles and their behaviours. Whilst conducting this review of literature a number of toolkits were repeatedly used by different organisations and studies. The most commonly used toolkits were: Monte Carlo N-particle Transport Code (MCNP) developed by Los Alamos National Laboratory, GEANT4 (**GE**ometry **AN**d **T**racking) developed by the European Organisation for Nuclear Research also known as CERN, and FLUKA developed by the Italian National Institute for Nuclear Physics (INFN). While MCNP is most frequently used to perform simulations for dosimetry and shielding, it can be used for detector design and particle tracking. GEANT4 and FLUKA are widely used in the nuclear and medical physics industries for their ability to track particles' passages through matter. FLUKA specialises in beam-machine interactions in the energy range MeV up to 10^5TeV (Böhlen *et al.*, 2014). This energy range is significantly higher than the diagnostic X-ray energy range (30keV – 100keV) (Bushberg & Leidholdt, 2002).The free software package GEANT4 is populated with tools which can accurately simulate the passage of particles through matter. Written in C++, GEANT4 is one of the only free Monte Carlo software packages that contains majority of the physical simulation processes. These include but are not limited to, system geometry, materials, particle generation and tracking and well validated nuclear physics models (Agostinelli *et al.*, 2003; Kippen, 2004; Zou *et al.*, 2010; Lenti and Veltri, 2011). GEANT4's comprehensive toolkits alongside its well validated physical models was why it was selected to perform this project's Monte Carlo Simulations.

2.4 Literature Review Gaps to be Addressed in Thesis

Currently one of the largest gaps in research found during the literature review is the lack of published research regarding the use of CSI for imaging the head region. More specifically no published studies were found during the literature review to have used CSI for stroke detection. The terms "Compton Scatter Imaging", "Compton Scatter Imaging Tissue", "Compton Scatter Imaging CT" and "Compton Scatter Imaging Stroke" on online databases such as PUBMED and the Institute of Physics and Engineering in Medicine was used to in

the search. Whilst CSI has been used in studies, for example Ryan *et al.* using CSI to image the breast region in 2005 and Redler *et al.* for the lungs in 2018, no CSI systems have been commercialised into a functioning, clinical, medical device. CSI, however, has been successfully commercialised for security applications. The application of CSI with a novel CT scanner geometry like the Micro-X CT Scanner has not been reviewed in the available published literature. Using similar approaches and methods outlined in previous soft tissue studies using CSI, such as Ryan *et al.* and Redler *et al.*'s work, this thesis investigated the use of CSI for the detection of strokes. Current research published in the scientific literature about CSI is performed through both physical and simulated testing methods. This thesis used simulations, in the form of Monte Carlo Simulations, due to a limited project budget and limited availability of physical testing materials required.

Chapter 3: Aim of Thesis

3.1 Project Aim

The aim of this project is to identify if Compton Scatter Imaging (CSI) can be a successful tool to assist in the detection of strokes. To answer the research question "Can Compton Scatter Imaging be incorporated with the Micro-X CT Scanner to aid in the detection of stroke?" the project goals outlined in 3.2 will be completed.

3.2 Project Goals
3.2.1 Literature search: Identify possible chemical differences between healthy, ischemic, and hemorrhagic brain tissue

This goal involves an extensive review of stroke pathophysiology literature to identify the chemical differences between healthy, ischemic, and hemorrhagic brain tissue on an atom and molecular level. The completion of this task will aid in material selection for data collection.

3.2.2 Calculations of Compton Scatter Cross-sections

This goal consisted of performing calculations of what the theoretical scatter signal would be. Compton scatter theory will be utilised to calculate the scatter cross-sections. The completion of this task will aid in identifying the data collection source and detector requirements.

3.2.3 Test Plan Development

Using knowledge gained from the completion of the first two goals, a test plan will be developed. This plan will include the phantom, detector, and source specifications.

3.2.4 Data Collection

Following the plan that will be outlined in the completion of goal three, Monte Carlo simulation environments will be built. X-ray projection data from ischemic, hemorrhagic, and healthy brain tissue will be collected in both traditional and Compton-scatter imaging set-ups.

3.2.5 Data Analysis

This goal will summarise the project's findings. Within this goal, MATLAB will be used to perform a comparison of the photon intensities where both a contrast and statistical analysis will be performed. These various methods will be applied in an attempt to quantify the differences in the images collected in chapter 7.

.

Chapter 4: Literature Search: Identifying Chemical Differences Between Healthy, Ischemic, and Hemorrhagic Brain Tissues

4.1 Objective

Perform a literature review to systematically review the current knowledge on the differences between healthy, ischemic and hemorrhagic brain tissues on an atom and molecular level.

4.2 Methods

A thorough and systematic literature search was executed to retrieve the current knowledge between the differences in stroke and healthy tissues. A web-based search was performed through the university databases MEDLINE, PubMed and ScienceDirect. Table 2 outlines the search terms, outcomes and papers selected. Literature will be excluded if articles are animal studies, treatment, post stroke, preventative or risk factor specific.

Table 2: Literature Search Term Outcomes from Stroke Physiology Literature Search

Types of Documents	Search Terms	Outcome
Articles 2001-2021	"Stroke Pathophysiology" AND molecular	<u>12 results</u> - *9 excluded, deemed irrelevant through title (post stroke morbidities pathophysiology or animal studies)* - *1 excluded, deemed irrelevant through abstract and results (in alternate language unable to translate)* 2 articles included in review
Book chapters 2001-2021	"Stroke Pathophysiology" AND molecular	<u>49 results</u> 49 book chapters from 3 books All 3 books deemed relevant - *41 chapters excluded, deemed irrelevant through title (treatments, epidemiology, preventative, and risk factors)* 8 chapters included in review
Articles 2001-2021	"Stroke Pathophysiology" AND ischemia	<u>24 results</u> - *2 articles already included in review* - *12 excluded , deemed irrelevant through title (post stroke morbidities pathophysiology, animal studies, treatments and epidemiology)* - *9 excluded, deemed irrelevant through results and abstract sections (pathophysiology past tPA stroke 4.5hour*

		onset window, not molecular – pathophysiology in terms of cerebral flow rates) 1 article included in review
Book chapters 2001-2021	"Stroke Pathophysiology" AND ischemia	<u>80 results</u> 80 book chapters from 3 books 3 books and chapter already in review - *8 chapters already included in review* - *66 chapters excluded, deemed irrelevant through title (treatments, epidemiology, preventative, and risk factors)* 6 chapters included in review
Articles 2001-2021	"Stroke Pathophysiology" AND hemorrhage	<u>13 results</u> - *3 already included in review* - *10 excluded, deemed irrelevant through title (post stroke morbidities pathophysiology or animal studies)* 0 articles included in review
Book chapters 2001-2021	"Stroke Pathophysiology" AND hemorrhage	<u>89 results</u> 89 book chapters from 4 books 2 books already in review 1 book deemed irrelevant, post morbidities - *5 chapters already in review* - *69 chapters excluded, deemed irrelevant through title (treatments, epidemiology, preventative, and risk factors)* - *13 chapter excluded, deemed irrelevant through book content (post stroke morbidities pathophysiology)* 2 chapters included in review

4.3 Results

Before discussing stroke pathophysiology in greater detail, it is to be noted that the molecular and cellular processes in strokes is a knowledge field that is still growing and expanding, and this review will contain the current medical consensus. The pathophysiology of ischemic stroke greatly differs from hemorrhagic strokes. Firstly, ischemia is when a blot clot disrupts the blood supply to the brain and hemorrhagic occurs when a broken blood vessel disrupts the blood supply to the brain (Hui, Tadi and Patti, 2021). The mechanisms of cell death are initiated in ischemic strokes through a number of processes but most notably through excitotoxicity, whereas inflammatory cascades initiate cell death in hemorrhagic strokes. The process of oxidative stress occurs in both types of strokes (Carroll and Chataway, 2006; Minnerup *et al.*, 2013; Yamashita and Abe, 2020). The pathogenesis of both strokes are

mapped out and compared in the flowchart in figure 4 and the pathophysiology is described in sections 4.3.1 and 4.3.2.

4.3.1 Ischemia Pathophysiology

During ischemia, when the blood supply is disrupted, a depletion in energy source Adenosine Triphosphate (ATP) leads to cell depolarisation from the failure of cell pumps which leads to an influx of calcium ions (Ca^{2+}) (Belrose *et al.*, 2012). This cell membrane depolarisation also causes glutamate to be released, which in turn further increases calcium ions and leads to cell death, and causes mitochondria dysfunction (Yamashita and Abe, 2020). The increase of calcium also initiates the release of fatty acids which creates an influx of free radicals, such as nitric oxide (NO), hydrogen peroxide (H_2O_2) and oxygen ions (O_{2-}), that indirectly lead to cell death through oxidative stress (Minnerup *et al.*, 2013). Calcium increases at almost every stage and mechanism of cell death in ischemia and it has been proven that the increase is greater than 100 times (Kristián and Siesjö, 1998; Minnerup *et al.*, 2013; Yamashita and Abe, 2020).

4.3.2 Hemorrhagic Stroke Pathophysiology

During hemorrhagic stroke, when the blood vessel breaks and the blood which escapes starts to pool together forming a hematoma (Aronowski *et al.*, 2015; Yamashita and Abe, 2020). The accumulation of blood in the hematoma causes sudden disruptions to the tissue, increases intracranial pressure, and decreases cerebral blood flow(Carroll and Chataway, 2006; Aronowski *et al.*, 2015; Yamashita and Abe, 2020). As the blood pools, roughly an hour after stroke onset, a molecule essential for blood coagulation, thrombin, is activated. The blood-brain barrier is degraded by the activated thrombin leading to neuronal cell damage. Neurotoxic components heme and iron are released as the body tries to breakdown the hematoma which is forming. Heme and iron cause the influx of free radicals NO, H_2O_2 and O_{2-} which results in cell death (Lee *et al.*, 2012; Lin and Selim, 2012; Yamashita and Abe, 2020).

4.3.3 Selection of Elements

After a thorough review of stroke pathophysiology, it was decided that organic elements, Hydrogen, Carbon and Oxygen would be selected to mimic healthy brain tissue. For simplicity in the models, 1 element was selected to represent the two types of stroke. One element would reduce computational times which are expected to be extremely long.

Due to the large 100-fold increase of calcium during ischemic strokes, calcium was selected to mimic ischemic brain tissue. Iron is found to increase during strokes by 45%, and also

contributes for the reason that blood is hyperdense on CT hemorrhagic stroke images, therefore iron will be selected to represent hemorrhagic stroke tissues.
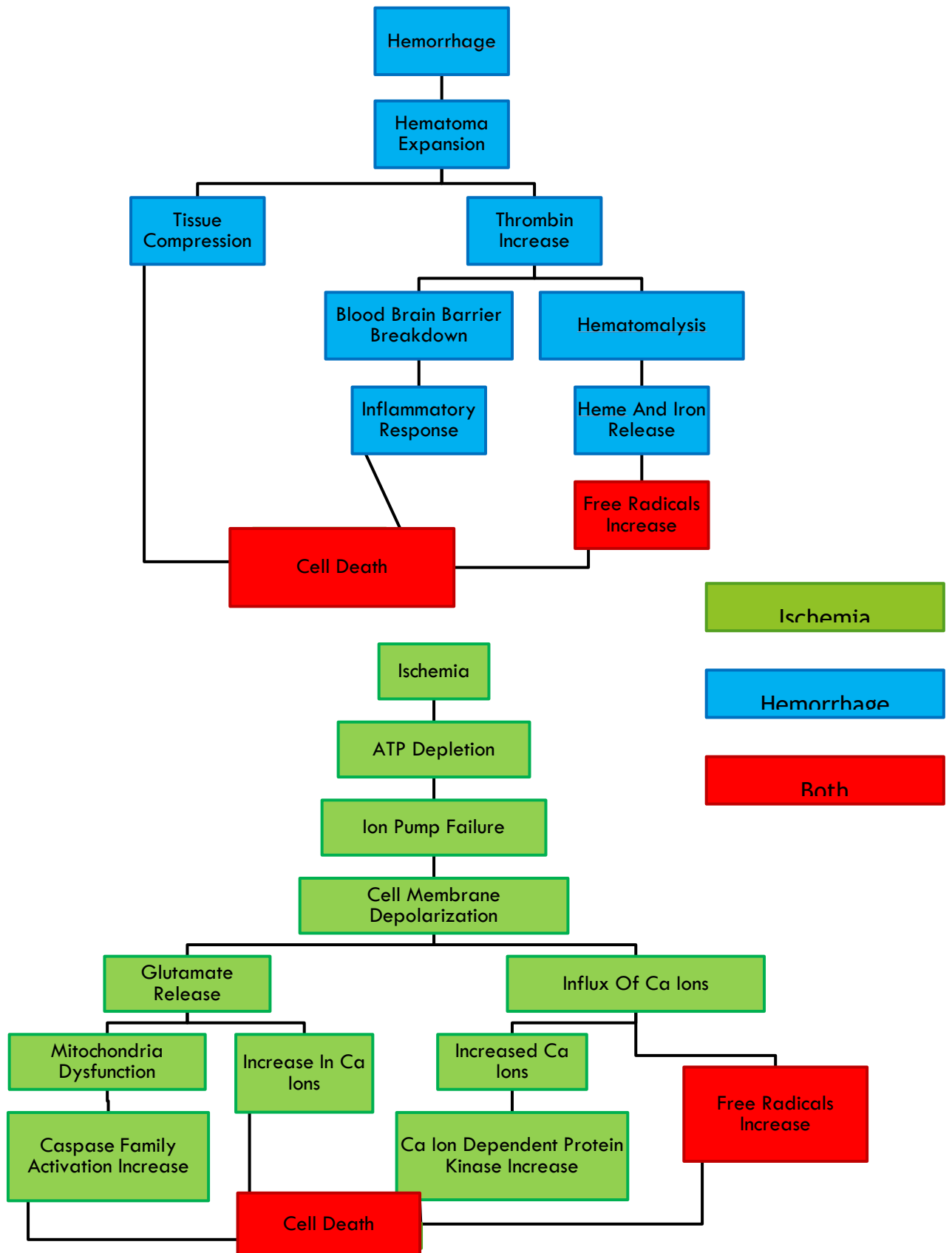
Figure 4: Comparison of pathophysiological mechanisms of cell death in ischemic and haemorrhagic strokes. Image drawn by Erica Nunn

Chapter 5: Calculations of Compton Scatter Cross-sections

5.1 Objective

Calculate the theoretical Compton Scatter Cross-sections and hypothesise the expected scatter signal changes.

5.2 Compton Scatter Theory

The inelastic scattering of a photon is known as Compton Scatter. During Compton Scatter, the incident photon is scattered through the angle θ.
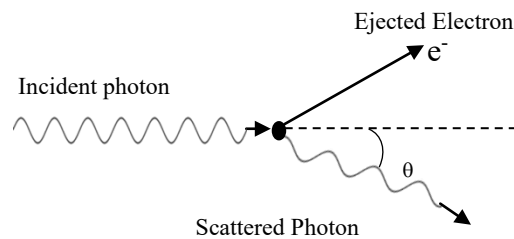
Figure 5: Compton Scattering Process. Image drawn by Erica Nunn

The photon's frequency decreases during this scattering. The change in frequency is described in equation 1. The Compton formula was derived assuming that photons have particle-like behaviour and observe the conservation of energy and momentum laws.

$$\Delta \lambda = \lambda' - \lambda = \frac{h}{m_0 c} \left(1 - \cos \theta\right) \qquad \text{Eq 1}$$

Equation 1: the Compton Formula

where λ is the wavelength of the incident photon, λ' is the wavelength of the photon after scattering, h is the Planck constant which h=6.626 x 10^{-31} J.s, m_0 is the electron rest mass where m_0= 511keV, c is the speed of light, θ is the scattering angle

Similarly, obeying the conservation of energy laws, the scattered photon energy can be calculated using equation 2.

$$E_s = \frac{E_0}{1 + \left(\dfrac{E_0}{m_0 c^2}\right)\left(1 - \cos \theta\right)} \qquad \text{Eq 2}$$

5.3 Compton Scatter Cross-Sections Theory

The Klein-Nishina (KN) differential scattering cross-section equation describes the probability of a photon scattered by an unbound electron at rest, through an angle θ, due to Compton scatter. KN is described in equation 3.

$$\frac{d\sigma_{KN}}{d\Omega} \cong \frac{r_e^2}{2}[1 + \cos\theta]\left[\frac{1}{1 + \alpha(1 - \cos\theta)}\right]^3 \left[1 + \frac{\alpha^2(1 - \cos\theta)^2}{(1 + \cos^2\theta)[1 + \alpha(1 - \cos\theta)]}\right] \quad \text{Eq 3}$$

Equation 3: KN Differential Scattering Cross-section Equation:

Where r_e is the classical electron radius and $r_e = \frac{e^2}{m_0 c^2} = 2.818 \times 10^{-15}$ m, Where $\alpha = \frac{E_0}{m_0 c^2}$, where $m_0 c^2 = 511 keV$ and E_0 is the incident photon energy.

In the scope of this project the electrons ejected during the Compton Scattering process will be bound to an atom. Thus, the equation needs to be modified to account for the extra electron binding energy. The probability of Compton Scatter interactions occurring reduces when electron binding energy is present. The KN equation can be multiplied with a corrective factor known as the incoherent scattering function, $S(x, Z)$. The incoherent scattering function is the probability that the most inner electrons with the greatest binding energy, the K-shell electrons, receive momentum from the incident photons. The total differential scattering cross-sections for electrons bound to an atom is given as:

$$\frac{d\sigma_c}{d\Omega}(\theta) = S(x, Z).\frac{d\sigma_{KN}(\theta)}{d\Omega} \quad \text{Eq 4}$$

Equation 4: Atom-Bound Scatter Cross-sections:

Where x is the momentum transfer and $x = -\frac{\sin\left(\frac{\theta}{2}\right)}{l(\AA)}$, θ is the scattering angle, $\lambda(\AA)$ is the photon wavelength in angstroms where $\lambda(\AA) = \frac{12398.52}{E_0}$, and E_0 is the incident photon energy in eV, Z is the Atomic Number, $\frac{d\sigma_{KN}(\theta)}{d\Omega}$ is calculated in equation 3

5.4 Differential Scatter Cross-sections

5.4.1 Klein-Nishina for single electron at rest

The likelihood and angular distribution of photons scattered from a singular electron at rest was calculated for X-ray photons in the Micro-X CT Scanner energy range, 40keV through to 100keV, using equation 3.
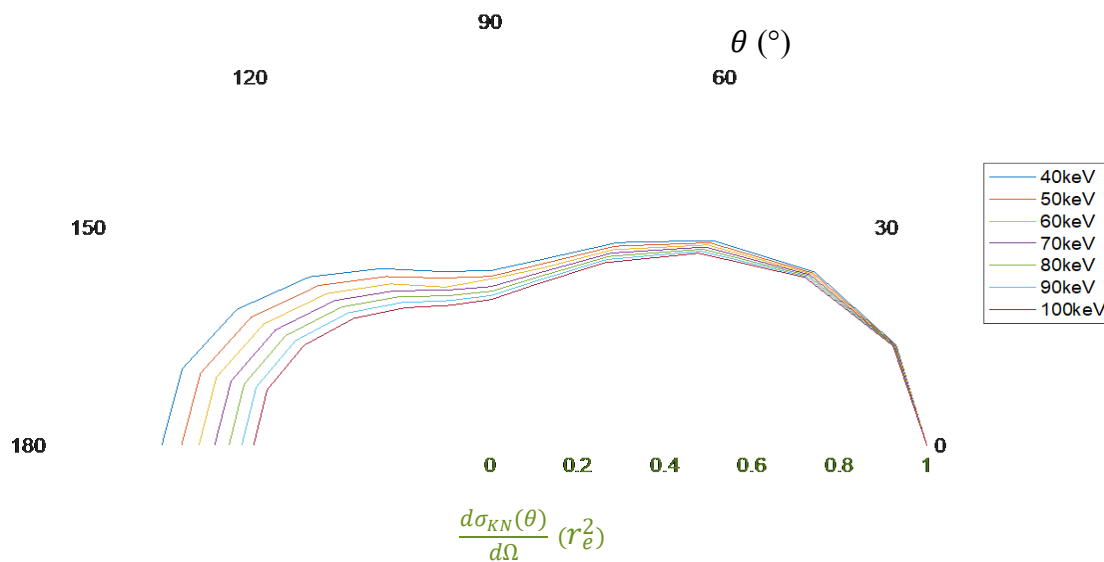
Figure 6: Differential Cross-Sections of Compton Scatter over 180 degrees, calculated using equation 3, where the cross-section is represented by a radius vector expressed in units of r_e^2. The cross-section represents the likelihood and angular distribution of scattered photons.

5.4.2 Atom-Bound Electrons Corrective Factor: The Incoherent Scattering Funtion

The incoherent scattering function is traditionally found through measuring physical data. Due to limited access to the correct standardised materials required for measuring the incoherent scattering function, the values were obtained from Hubbell *et al.*'s extensive atomic study in 1975. Hubbell *et al.* work is widely cited in over 1000 academic works and is widely regarded as the industry standard for the Incoherent Scattering Function. Hubbell *et al.* presented the incoherent scattering function for all elements with atomic number 1 to 100.

The table in Hubbell *et al.*'s work is presented is in the form of S(x,Z), where $x = -\frac{\sin\left(\frac{\theta}{2}\right)}{l(\text{Å})}$, $l(\text{Å}) = \frac{12.39852}{E_0}$ and E_0 is the incident photon energy in keV. To obtain the correct values needed, the appropriate *x* values for angles 0° through to 180° and energies 40keV to 100keV had to be calculated. Example of the *x* calculations can be found in table 3 for 40keV and the complete exhaustive calculations can be found in the appendix 13.2.

Table 3: Calculation of x value of the Incoherent Scattering Function

θ	$\sin\dfrac{\theta}{2}$	$l(\text{Å}) = \dfrac{12.39852}{40}$	$x = \dfrac{\sin\dfrac{\theta}{2}}{l(\text{Å})}$
15	0.1305	0.309963	0.42110249
30	0.2588	0.309963	0.83499981
45	0.3827	0.309963	1.23461004
60	0.5000	0.309963	1.61309576
75	0.6088	0.309963	1.96398096
90	0.7071	0.309963	2.2812619
105	0.7934	0.309963	2.55950981
120	0.8660	0.309963	2.79396381
135	0.9239	0.309963	2.98061231
150	0.9659	0.309963	3.1162617
165	0.9914	0.309963	3.198591
180	1.0000	0.309963	3.22619151

5.4.3 Differential Scatter Cross-Sections for Hydrogen, Carbon, Oxygen, Calcium, and Iron

The differential scatter cross-sections for all 5 selected materials were calculated for the Micro-X CT Scanner energy range 40keV through to 100keV. The calculations were done using equation 4. The results were plotted on polar plots with the cross-sections represented by a radius vector expressed in units of r_e^2, the classical electron radius, 2.82×10^{-15} m (Del Guerra *et al.*, 1982). Differential Scatter Cross-Sections for 40keV and 100keV are depicted in figure 8 and 9. The complete set of Differential Scatter Cross-Sections are in Appendix 13.4.

The analysis of the Scatter Cross-Sections results will analyse the graph at 90°<θ<180°. An explanation for this is given in section 6.5 during the discussion of detector placement. At an energy of 40keV, the Differential Scatter Cross-Section is larger for the healthy tissue elements compared with both ischemic and hemorrhagic tissue elements. The difference in

the Differential Scatter Cross-Sections is largest at a source energy of 40keV. Comparatively at 100keV, all tissue elements have the extremely similar Differential Scatter Cross-Sections. From these results its hypothesised that at 40keV when the X-rays reach the ischemic and hemorrhagic tissue, they are less likely to scatter compared with healthy tissue. This would result in less scatter photons at the detector from ischemic tissue compared with healthy tissue and a change on contrast will be seen in the output image. At 100keV it is hypothesised that no change in image intensity would be seen between the healthy, ischemic, and hemorrhagic tissues.
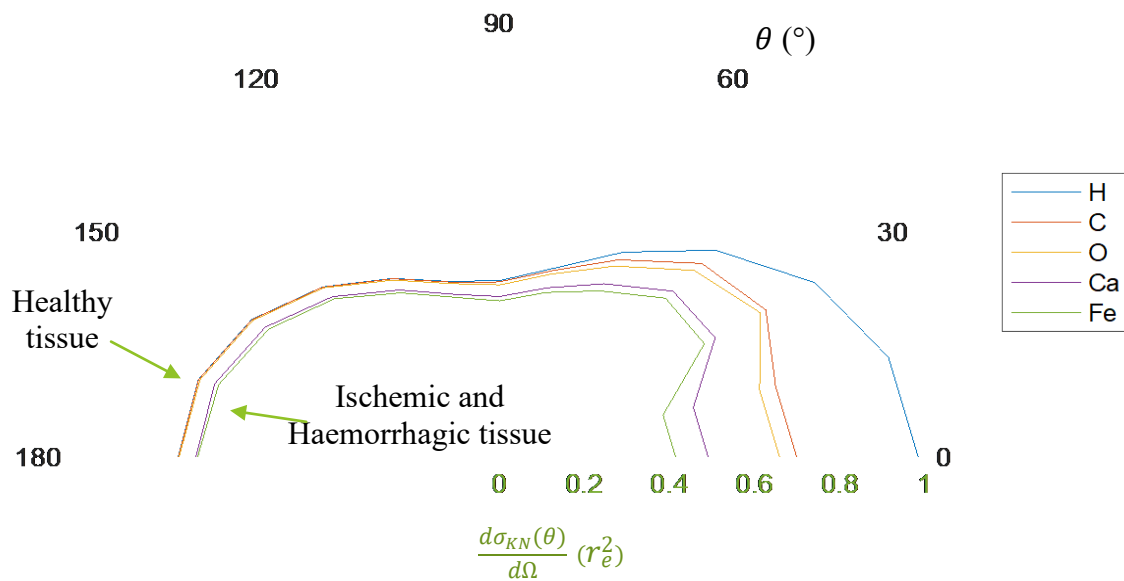
Figure 7: Differential Cross-Sections of Compton Scatter for the 5 selected materials, Hydrogen, Carbon, Oxygen, Calcium, and Iron, over 180 degrees at 40keV.

Calculated using equation 4, where the cross-section is represented by radius vector expressed in units of r_e^2. The cross-section represents the likelihood and angular distribution of scattered photons.

Differential Scatter Cross-Section at 100keV
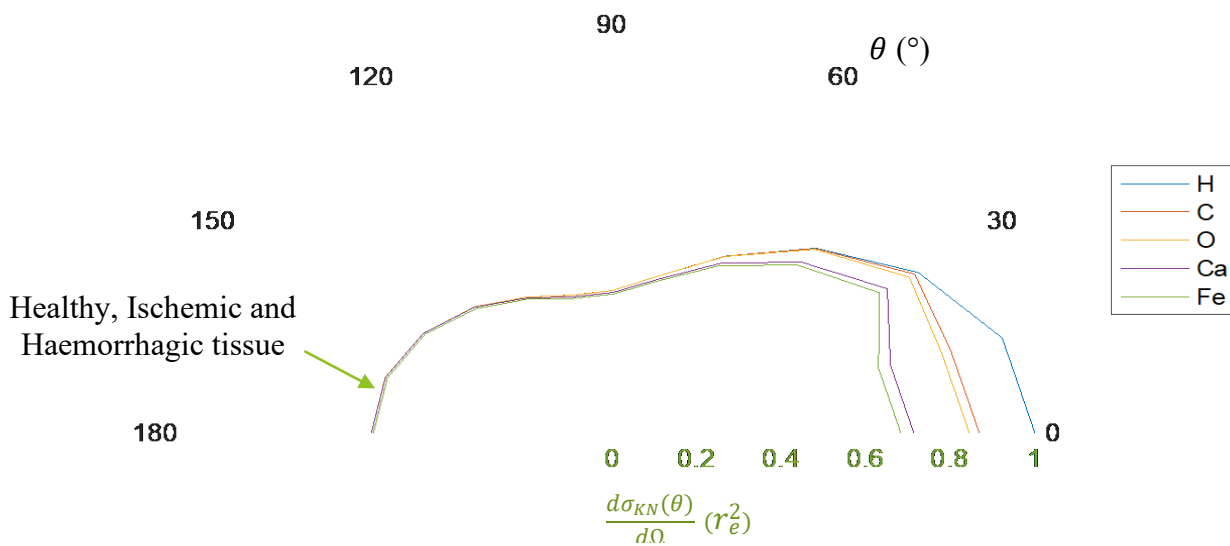
Figure 8: Differential Cross-Sections of Compton Scatter for the 5 selected materials, Hydrogen, Carbon, Oxygen, Calcium, and Iron, over 180 degrees at 100keV.Calculated using equation 4, where

the cross-section is represented by radius vector expressed in units of r_e^2. The cross-section represents the likelihood and angular distribution of scattered photons.

Chapter 6: Test Plan Development

6.1 Objective

Create a test plan that includes the phantom, detector, and source specifications.

6.2 Method

Use results from chapter 4 to determine the phantom specifications. Derive the detector and source specifications from chapter 5 results.

6.3 Phantom Specifications

The phantom for simulations was chosen to be an adapted Shepp Logan phantom. The traditional Shepp Logan phantom can be seen in figure 9A. The adapted stroke phantom chosen (figure 9 B) had 3 regions: skull, brain and injured site. The dimensions of the phantoms can be found in appendices 13.5. The phantom in figure 9 C is a healthy (control) phantom, to which the results from the stroke phantom will be compared.
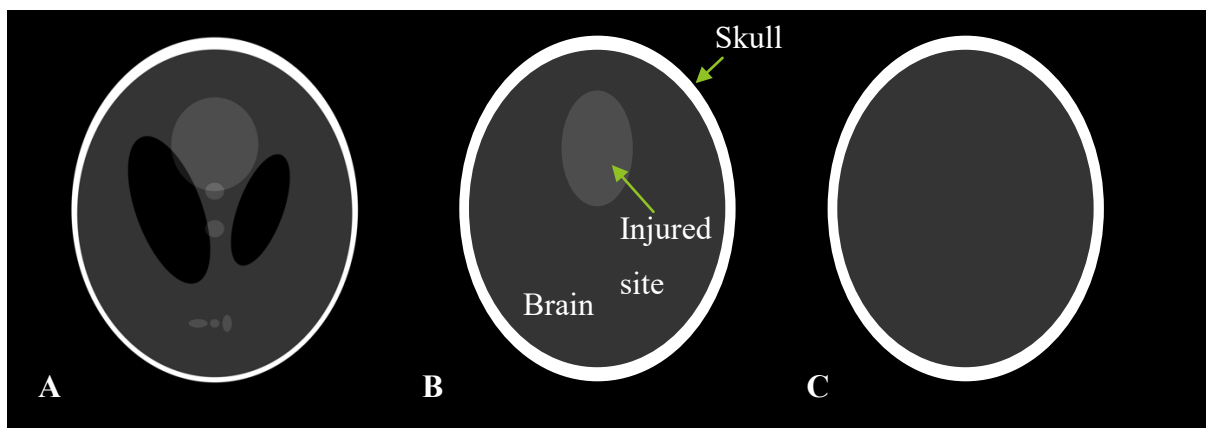
Figure 9: Simulation Phantoms A: Shepp-Logan, B: Adapted Stroke Phantom, C Healthy Phantom.

6.4 Source Selection

The results in chapter 5 outlined that the greatest expected difference in scatter is at 40keV. Therefore, 40keV was selected as the source beam energy. Whilst the Micro-X CT Scanner uses a carbon nano X-ray tube which emits a polychromatic X-ray beam, the source in the scope of this project will be assumed to be a monochromatic beam.

6.5 Detector Placement
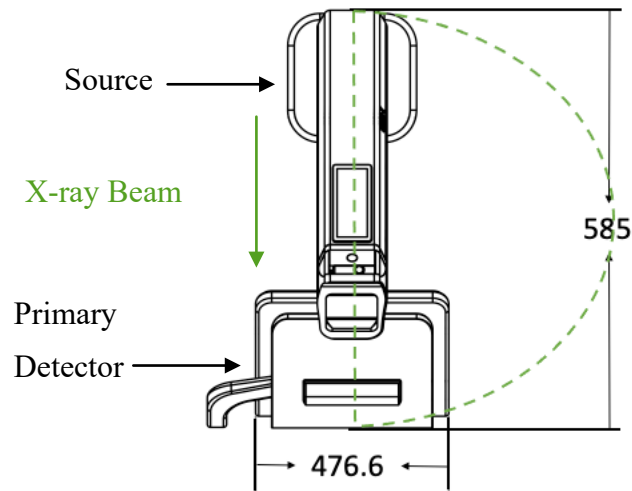
Figure 10: Secondary Detector Possible Placements for CSI. Image Drawn by Erica Nunn
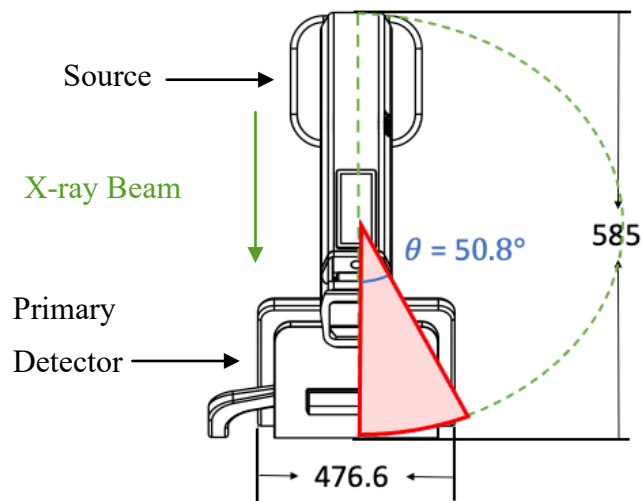
Figure 11: Current Micro-X System Where Red Zone Depicts Where A Secondary Detector Can Not be Placed. Image Drawn by Erica Nunn

The secondary detector for Compton scatter imaging can be placed anyway along the green dotted arch in figure 10. However, the current Micro-X CT Scanner geometry is still in its initial design phase. It is expected that the device geometry, in regard to detector size, will be subjected to changes during the iterative design phases that are currently being undertaken. For example, in the current system shown in figure 11, the red triangle denotes the angular zone $0° < \theta < 50.8°$, where an extra detector cannot be placed due to the Micro-X CT Scanner's current detector used for the traditional CT imaging. Figure 12 depicts the changes in the red

zone, the area a secondary detector for the CSI system can not be placed, at differing varying detector sizes.
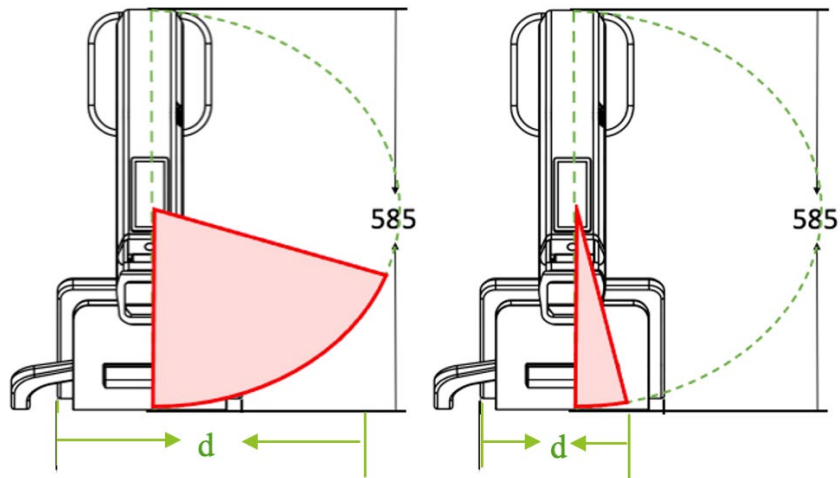
Figure 12: illustration of when the detector size, denoted as d in images,increases, the area where a CSI detector can not be placed increases. Likewise, when the detector size decreases, this area decreased. Image Drawn by Erica Nunn

Therefore, a detector placement of $90° < \theta < 167°$ was investigated. This region of detector placement is depicted in the green arch in figure 13 which considers the placements of the source and primary detectors.
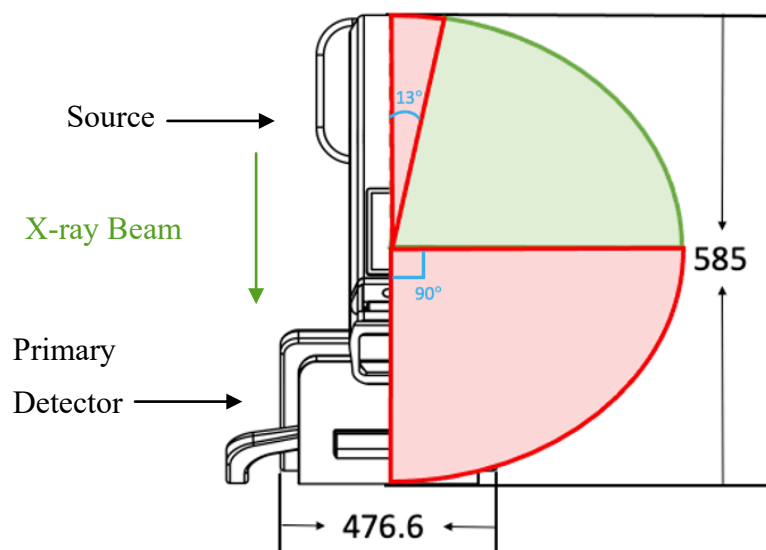
Figure 13: Green zone depicting where a secondary detector can be placed to add CSI to the Micro-X CT Scanner. Image Drawn by Erica Nunn

Looking at the results from the calculated differential scatter cross-sections completed in chapter 5, the difference in the expected scatter signal is found to be greatest at 150 degrees, see table 4. This was calculated using equation

$$\frac{|d\Omega_H - d\Omega_S|}{\frac{d\Omega_H + d\Omega_S}{2}}$$
Eq 5

Equation 5:The Percentage Difference between two values

Where $d\Omega_H$ is the cross-section value for healthy tissue and $d\Omega_S$ is the cross-section value for stroke tissue

Since $d\Omega_H$ indicates likelihood of scatter, the larger the percentage difference between the healthy and stroke values at a certain angle, the larger the difference in photons reaching the detector at that position is to be. It is expected that the change in contrast between healthy and stroke tissue will be at its greatest with a detector placement at 150 degrees.

Table 4: Detector Placement Justification. Calculations can be found in appendix 13.6

Angle°(θ)	Difference between healthy and ischemic tissue scatter (%)
120	5.23
135	5.37
150	**5.43**
165	5.39

It is noted that smaller steps over a span of 45 degrees would be more precise in finding the optimum detector placement. Larger steps, of 15 degrees, was selected as the detectors selected have a large area which would capture X-rays with trajectories of multiple angles.

Chapter 7: Data Collection

7.1 Objective

Using Monte Carlo Simulations, collect X-ray projection data from ischemic, hemorrhagic, and healthy brain tissue in both traditional and Compton-scatter imaging set-ups.

7.2 Methods

The data collection was performed using the GEANT4 toolkit. The GEANT4 simulations followed the computational flow chart in figure 14. Each simulation was run 10 times to reduce the likelihood of errors and improve system accuracy. The average run time of the simulations was 96 minutes. 10 times was selected to keep the total data collection time within the 4 weeks of dedicated project time.
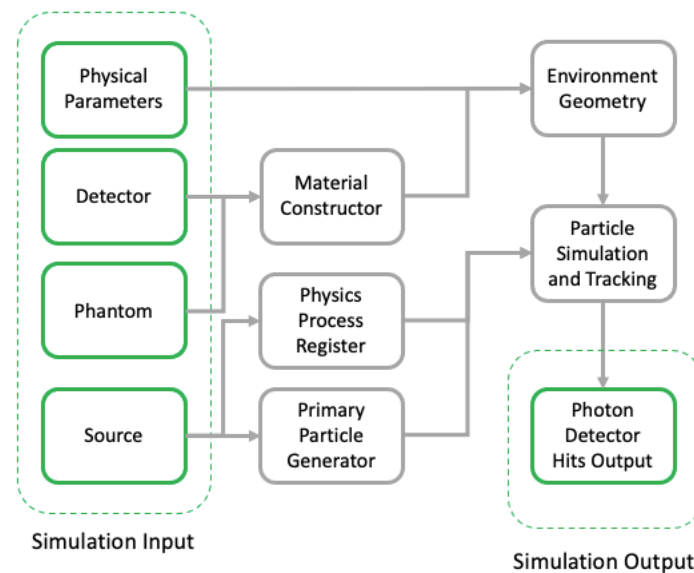
Figure 14: Computational flowchart of the GEANT4 Simulations

The simulation environment consisted of 4 major components; scanned object, detector, X-ray generation and physical parameters. The details for the components are described in table 5. The setup of the Compton Scatter Imaging simulation consisted of a phantom with an iso centre positioned (0,0,0) and a monochromatic cone beam source of 40keV placed 425mm from the phantoms iso centre. Whilst X-ray tubes in the physical world produce a polychromatic beam, for simulation simplicity and reduction of computational time, a monochromatic source was selected. In the physical world a tube voltage of approximately 70kVp would be required to obtain an average beam energy of 40keV (Hubbell *et al.*, 1975).

A detector is placed 150° offset from the phantom at a distance of 850mm from the phantom iso centre and 736mm from the source. A pinhole collimator, with an aperture of 1mm, for the detector is placed between the detector and phantom at 425mm and 150° from the phantom iso centre. The simulation environment is depicted in figure 15.

Table 5: 4 major simulation components and their parameters for Compton Scatter Imaging System

Xray		Phantom		Detector		Physical Parameters	
Beam type	Cone Beam	**Materials**	Bone, Brain Grey/White Matter, Blood whole, Ischemic Soft Tissue	**Geometry**	200 x 140 pixels Pixels 1x1mm	**Source to iso-centre**	425mm
Energy	40keV	**Shape**	a b	**Detector Type**	Caesium Iodide Scintillator	**Source to detector**	150° 736mm
		Size	a:174.8 mm b:131.1mm			**Detector to iso-centre**	850mm
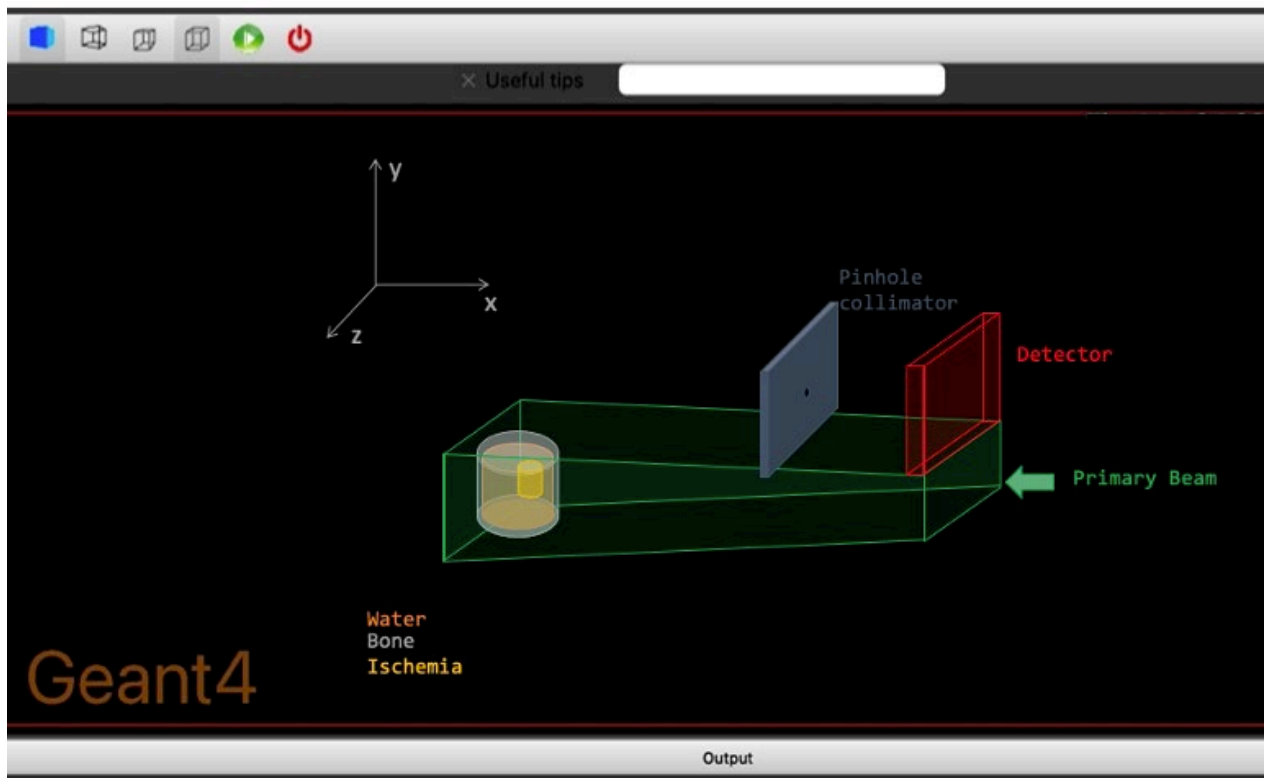
Figure 15: Screenshot of Simulation Environment for CSI system.

Table 6: 4 major simulation components and their parameters for Traditional Imaging System

Xray		Phantom		Detector		Physical Parameters	
Beam type	Cone Beam	**Materials**	Bone, Brain Grey/White Matter, Blood whole, Ischemic Soft Tissue	**Geometry**	200 x 140 pixels Pixels 1x1mm	**Source to iso-centre**	425mm
Energy	40keV	**Shape**	a b	**Detector Type**	Caesium Iodide Scintillator	**Source to detector**	585mm
		Size	a:174.8 mm b:131.1mm			**Detector to iso-centre**	160mm

The setup of the traditional system is the same as the Compton system for the phantom and source placement. The only changes are the detector location. The detector centre is located

at (-160,0,0). Figure 16 depicts the simulation environment for the traditional imaging system setup.
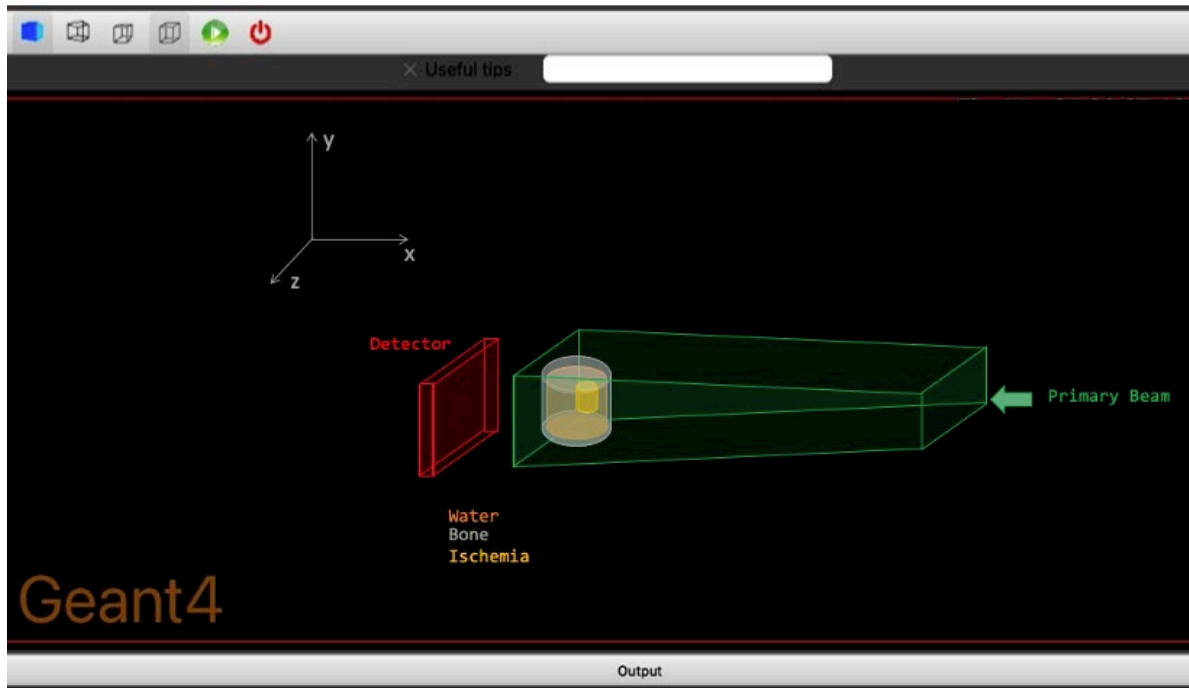
Figure 16: Screenshot of Simulation Environment for Traditional X-ray System

Interactions of the photons from the source and the electrons in the phantoms were simulated by the open sourced GEANT4 physics models. Photons were tracked through the two simulation setups described. When the tracked photons hit the detector, the location of the hit in relation to the detector geometry was recorded. At the end of the simulation the data were collected as a 2D matrix. The image matrix is composed of columns (M) and rows (N) that corresponded with the location of the pixels of the detector. The numbers (counts) in this matrix were the number of photon hits at the detector location (M_x,N_x).

Chapter 8: Data Analysis

8.1 Objective

This section analyses the data obtained from the Monte Carlo Simulations completed in chapter 7. This section aims to quantify if there is a difference in the stroke images compared with the healthy images using CSI.

8.2 Methods

Various methods will be applied in an attempt to quantify the differences in the images collected in chapter 7. All image analysis was performed using MATLAB.

8.2.1 Comparison of Photon Intensities
Contrast analysis

Each image obtained from the detector is the photon intensity, z_1 (stored as an unsigned integer value, in 16 bit), at detector pixel (x_1, y_1). To compare the photon intensities from each X-ray projection image, a region of interest (ROI) is selected using the matrices when imported to MATLAB. The mean and standard deviation of the photon intensities in that ROI is calculated. The mean intensities can be used in the Michelson equation (Pogson *et al.*, 2013) to find the contrast between the two ROI. The Michelson test is used as it quantifies the relative amount by which the ROI stands out.

$$contrast(\%) = 100 \times \frac{I_1 - I_2}{I_1 + I_2}$$

Equation 6: Michelson Contrast Equation
where I_1 & I_2 are the Means of the 2 ROI being compared

Statistical analysis

Firstly, a normality test (Shapiro-Wilk test) using software "GraphPad Prism" was performed on all the data (intensities in the healthy, ischemia and hemorrhage ROIs, for both the traditional and the CSI systems) to verify if these were normally distributed. The Shapiro-Wilk test operates by examining how close the sample data fits to a normal distribution.(King and Eckersley, 2019). If the data pass the normality tests, Confident Intervals can be used to determine whether the difference between two means is statistically significant,. Using the mean and standard deviation values calculated in MATLAB, the standard error, 95% Confidence Interval, t-statistic and significance level can be calculated to make such

comparisons. Initially the pooled standard deviation of the two tissues being compared is calculated using equation 7

$$s = \sqrt{\frac{(n_1 - 1)s_1^2 + (n_2 - 1)s_2^2}{n_1 + n_2 - 2}}$$

Equation 7: Pooled Standard Deviation Equation

where s_1 and s_2 are the standard deviations of the two samples with sample sizes n_1 and n_2.

Then the standard error of the difference between the two means being compared, $se(\overline{x_1} - \overline{x_2})$, was calculated using equation 8.

$$se(\overline{x_1} - \overline{x_2}) = s \times \sqrt{\frac{1}{n_1} + \frac{1}{n_2}}$$

Equation 8: Standard Error of the Difference between two means, $\overline{x_1}$ & $\overline{x_2}$

The P-value is calculated using a t-test calculator where the t value is calculated in equation 9.

$$t = \frac{\overline{x_1} - \overline{x_2}}{se(\overline{x_1} - \overline{x_2})}$$

Equation 9: T value Equation

When the P-value is less than 0.05, it can be concluded that the two mean values are significantly different. The P-value is obtained through a lookup table (Krzywinski and Altman, 2013).

8.2.2 Edge Detection

Results and changes in radiology need to be presented in a form that health practitioners can visually see difference. This is applied to enhance the changes in the images. The image processing technique, edge detection, for finding object boundaries within images, was applied to the images. Edge detection was applied in an attempt to detect discontinuities in contrast in the images. MATLAB was used for edge detection. A Fuzzy Logic Image Processing technique, where breaks in uniform regions are located using the image's gradients, was applied. The algorithm is described by the block diagram in figure 17.
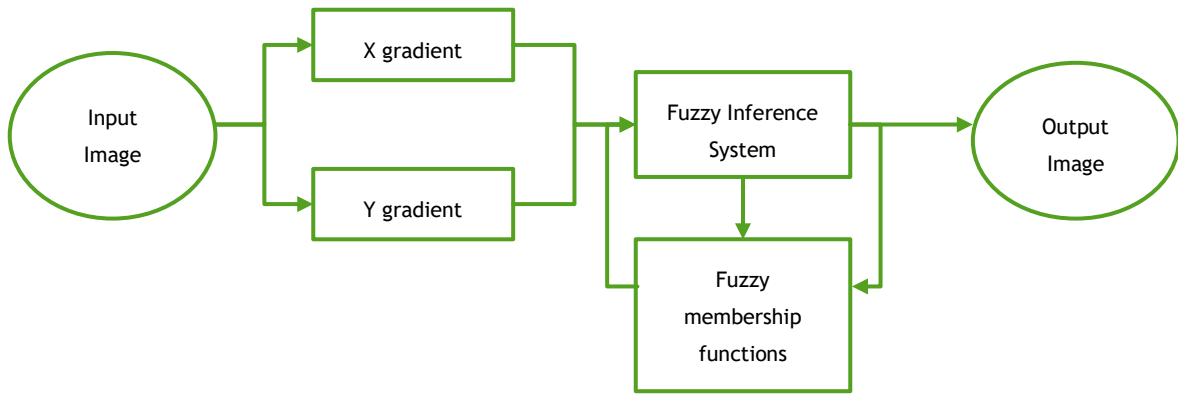
Figure 17: Fuzzy Logic Edge Detection Algorithm Approach

Firstly, the image data is converted to a double array. Gradient filters were applied to calculate the image gradient along the x and y axis. These calculated image gradients are used as inputs to the fuzzy logic algorithm. The fuzzy logic edge detection algorithm uses a Fuzzy Inference System which for each input, creates zero-mean gaussian membership functions, $g(x) = e^{-\frac{(x)^2}{2s^2}}$ where s is the standard deviation. Increasing s makes the algorithm less sensitive to edges in the image. Triangular membership functions, white and black, are defined in the Fuzzy Inference System. The rules of the Fuzzy Logic Edge Detection Algorithm are defined as:

If :

$$I_x = 0 \ \& \ I_y = 0 \ \rightarrow I_{out} = white$$

$$I_x \neq 0 \ \ or \ \ I_y \neq 0 \ \rightarrow I_{out} = black$$
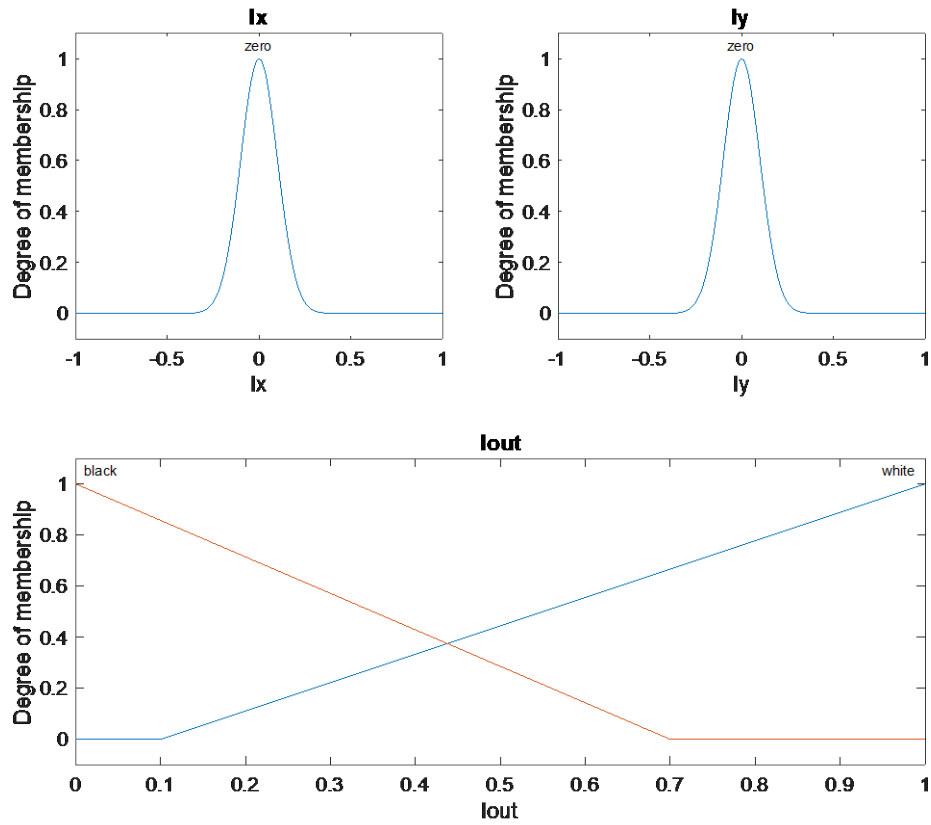
Figure 18: Fuzzy Logic Edge Detection Algorithm membership functions

8.3 Results

The 10 Image matrixes, for each simulation, were obtained, averaged and plotted in MATLAB to display the images. The greyscale of the images is scaled to the pixel values in the image matrix. The resulting images produced from simulations are presented in figure 19.
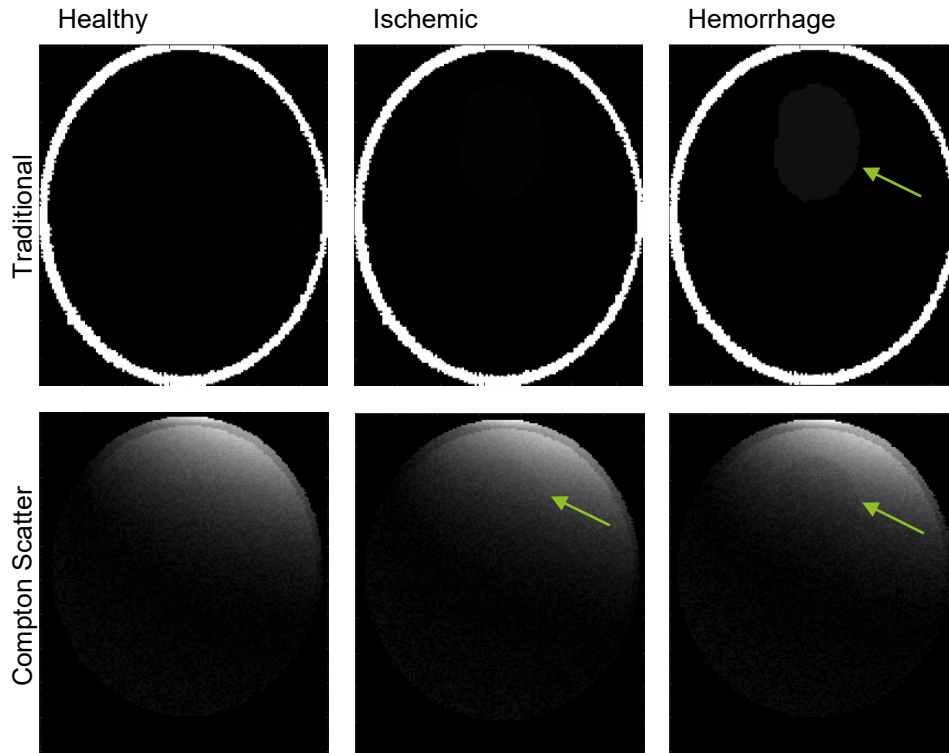
Figure 19: Simulation Averaged Output Images. Top row: healthy, ischemic and hemorrhage, X-ray projection images from a traditional X-ray system set up. Bottom row: output X-ray projection images from the Compton Scatter Imaging system set up with the healthy, ischemic and hemorrhage phantoms. The green arrows point to changes in contrast where the stroke injured site is.

It was expected in the traditional X-ray simulation images that a change in contrast (a lighter grey region) would be seen in the brain area but limited change in the contrast seen in the ischemic phantom simulations in the traditional X-ray system (brain region remain same colour). It was expected that a change in the contrast (darker grey region) would be seen in both the ischemic and hemorrhage simulations in the CSI system.

The results obtained in figure 19, the changes in contrast are difficult to see. Changing the images plotting greyscale, made the change in contrast in the hemorrhagic images easier to decipher (figure 20). The limited contrast change seen in the ischemic image from the traditional X-ray system is expected due to the fact that current X-ray systems do not see large differences in the contrast during acute ischemia (Kurz *et al.*, 2016). The change in greyscale scale did not cause ischemia in the CSI image to be more clearly identified. A change in the ischemia image is more clearly seen in the image in figure 19 where changes in the greyscale have not been made.
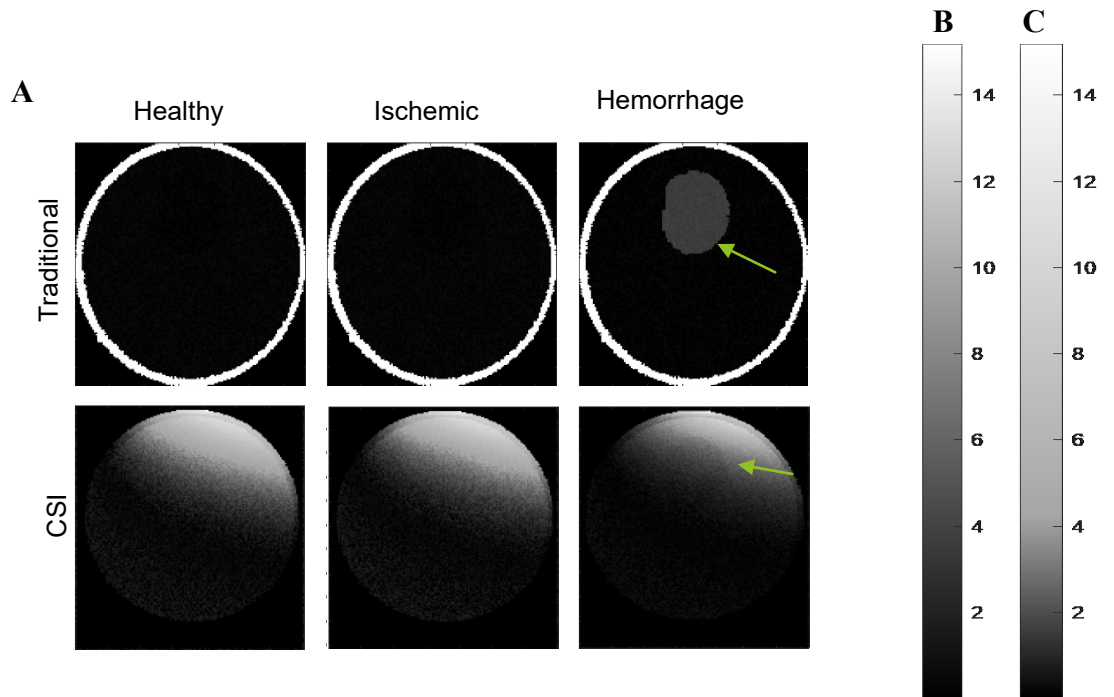
Figure 20: 20A: Resulting X-ray projection images when contrast scale changes from B to C

8.3.1 Comparison of Photon Intensities

The region of interest selected was an 11 x 11 pixel region depicted in figure 21. This region was selected in MATLAB.
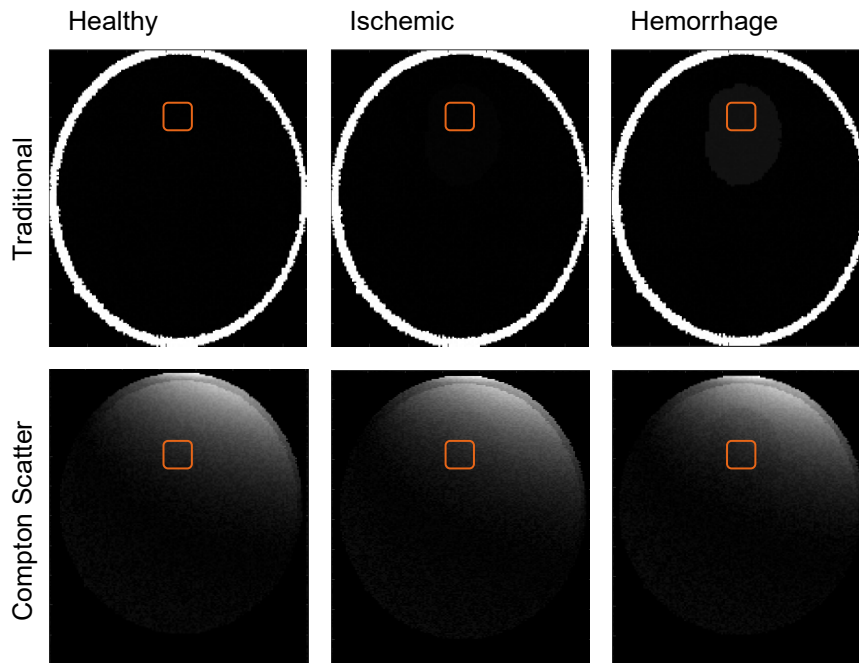
Figure 21: Selected Region of Interest

8.3.1.1 Normality Test

The results of the Shapiro-Wilk tests performed in GraphPad Prism (figure 22), showed that

all the intensity data were normally distributed (all p-values were greater than 0.05).

	Traditional			Compton Scatter	
Healthy	**Shapiro-Wilk test**			**Shapiro-Wilk test**	
	W	0.9335		W	0.7391
	P value	0.6076		P value	0.2495
	Passed normality test (alpha=0.05)?	Yes		Passed normality test (alpha=0.05)?	Yes
	P value summary	ns		P value summary	ns
Ischemic	**Shapiro-Wilk test**			**Shapiro-Wilk test**	
	W	0.807		W	0.5782
	P value	0.239		P value	0.0982
	Passed normality test (alpha=0.05)?	Yes		Passed normality test (alpha=0.05)?	Yes
	P value summary	ns		P value summary	ns
Hemorrhage	**Shapiro-Wilk test**			**Shapiro-Wilk test**	
	W	0.6932		W	0.2931
	P value	0.3948		P value	0.1098
	Passed normality test (alpha=0.05)?	Yes		Passed normality test (alpha=0.05)?	Yes
	P value summary	ns		P value summary	ns

Figure 22: Results of the normality test (Shapiro-Wilk test) performed on the intensity values in the healthy, ischemic and hemorrhage ROIs, for both the traditional and the CSI systems.

8.3.1.2 Statistical Analysis

After the normality tests, the mean and standard deviation of the intensities were calculated using the inbuilt MATLAB functions mean2 and std2 (table 7).

Table 7: Mean and Standard Deviation of the intensities within the selected healthy, ischemia and hemorrhage ROIs for both X-ray system types

	System			
	Traditional		**Compton Scatter**	
Tissue	**Mean**	**Std dev**	**Mean**	**Std dev**
Healthy	34.86	2.65	2.67	0.27
Ischemia	33.94	3.02	2.57	0.26
Hemorrhage	95.13	2.92	2.45	0.25

Using equations described in equation 6 through to 9 the contrast percentage, Standard Error, Confidence Interval, T-Statistic and Significance level of difference was calculated and presented in table 8. A p-value less than 0.05 is considered statistically significant. In the CSI system, the intensities for the ischemia and hemorrhage ROIs are both significantly different compared to the healthy ROI (P = 0.007 and P<0.0001 respectively). In the traditional

system, only the hemorrhage ROI was significantly different compared to the healthy ROI (P < 0.0001), whereas the ischemia ROI was not different from the healthy ROI (P = 0.7428).

Table 8: results of equations 6 Through to 9

Healthy Tissue compared with	System			
	Traditional		Compton Scatter	
	Ischemia	Hemorrhage	Ischemia	Hemorrhage
Contrast (%)	0.11%	46.36%	2.06%	4.33%
Difference	0.12	60.27	0.118	0.222
Standard error	0.365	0.358	0.034	0.034
95% CI	-0.5995 to 0.8395	59.5638 to 60.9762	0.0502 to 0.1860	0.1550 to 0.2890
t-statistic	0.329	168.13	3.425	6.529
P-value (t-test)	P = 0.7428	P < 0.0001	P = 0.0007	P < 0.0001

8.3.2 Edge Detection

Applying the edge detection algorithm to both ischemia and hemorrhage images from the Compton Scatter System returned extremely noisy images (figure 23). The edge of the injured site is not clearly defined in these images.
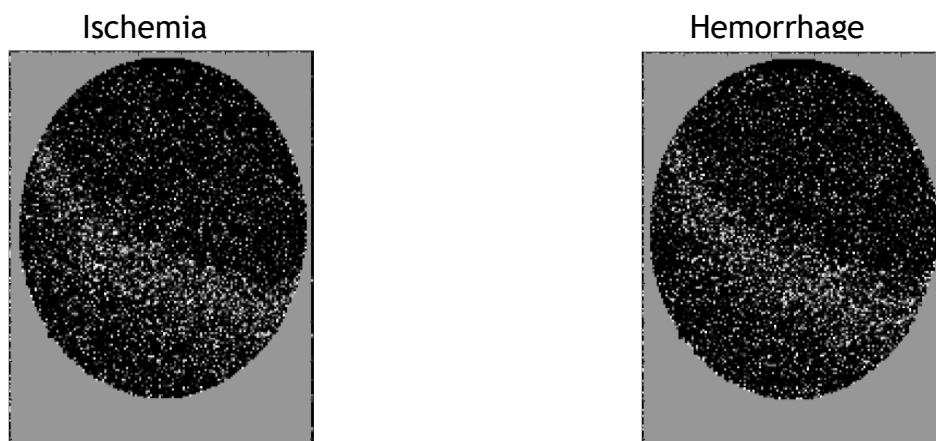
Figure 23: Edge Detection

In an attempt to de-noise the images, two different filters were applied. Firstly, a Gaussian filter was applied. Gaussian filters are smoothing filters which blurs the image and reduces

37

the noise. Wiener filter was also applied. The Wiener filter is an adaptive low-pass filter which attempts to remove noise in the images (Chen *et al.*, 2006). It is suspected that the noise in the image is the major contributing reason as to why the edge detection algorithm was unable to find definitive edges of the injured sites. Gaussian and Wiener filters are commonly regarded as extremely successful in de-noising images (Chen *et al.,*2006) and thus were selected to remove and filter this noise.
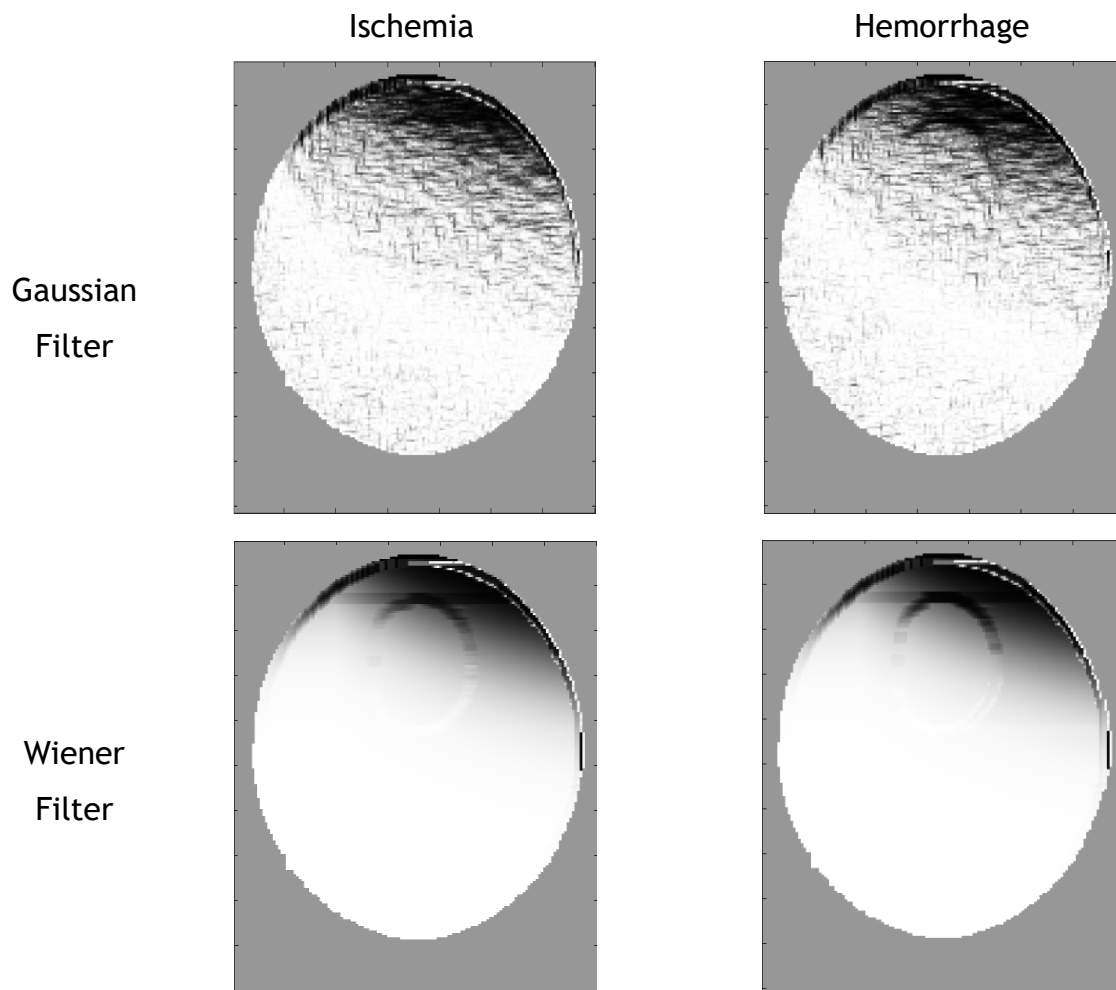
Figure 24: Edge Detection with noise reduction

Applying the Gaussian filter a more defined edge can be seen in the hemorrhage image but less defined in the ischemic image. The application of the Wiener filter with the edge detection algorithm has defined edges in both ischemic and hemorrhagic images. These results indicate that with the addition of image processing techniques to the raw system data, the CSI data become more appropriate for how medical practitioners intend to use radiological data. Further study into characterising the noise will need to be completed as

well as ensuring image processing techniques do not compromise the image integrity. The filters applied did not have filter parameters specific for the X-ray noise data, rather the suggested inbuilt filter parameters were used.

Chapter 9: Discussion

In this thesis CSI data was modelled using Monte Carlo Simulations. The Monte Carlo Simulations were built to determine if hemorrhagic and ischemic strokes can be identified using CSI. A Traditional X-ray imaging system was also modelled in the Monte Carlo simulations so the resulting images could be compared. While hemorrhage was seen in the traditional data (lighter grey area in the brain, figure 20) no ischemic region was seen. Comparatively ischemic and hemorrhagic regions were harder to decipher in the CSI. Performing a statistical analysis, it was found that the mean photon intensities in the simulation projection X-ray data were statistically different for the CSI hemorrhagic and ischemic and traditional hemorrhagic regions compared with the healthy tissue regions.

It should be noted however there are a number of limitations in regard to these results. Firstly, all simulations were completed with a monochromatic beam, to reduce computational time of the simulations, whilst CSI in the physical world would be completed with a polychromatic X-ray tube. A polychromatic X-ray beam would result in the head being irradiated with a spectrum of X-rays. Since the likelihood of scatter is proportional to the energy, it can be expected that imaging with a spectrum of X-ray energies will change the scatter produced by the tissues.

Secondly, these results do not consider the occurrence of multiple scattering within the tissue samples. The occurrence of multiple scattering is expected to add noise to the images. Multiple scattering has been investigated by numerous CSI studies. Huddleston, Bhaduri and Weaver in 1979, Del Guerra *et al.* in 1982 and Jones *et al.* in 2018 found multiple scattering caused blurring in the images. Jones *et al.* suggested increasing the angle between source and detector decreased the relative contribution of multiple scattered photons. Comparatively, Battista, Santon and Bronskill (1977) suggest a dual energy subtraction algorithm would be capable to derive a scatter signal free from multiple scatter.

Taking a line profile, figure 25, of the simulation output images from the CSI system showed an exponential drop in intensity. It is theorised that this exponential drop is caused by the attenuation of the primary source beam. Battista, Santon and Bronskill in 1977 suggested two attenuation correction techniques for CSI. Firstly, physical methods including Compton Scatter Tomography, a primary source beam with a higher energy or additional detectors to monitor the primary attenuation. The secondary technique is an iterative attenuation correction algorithm.
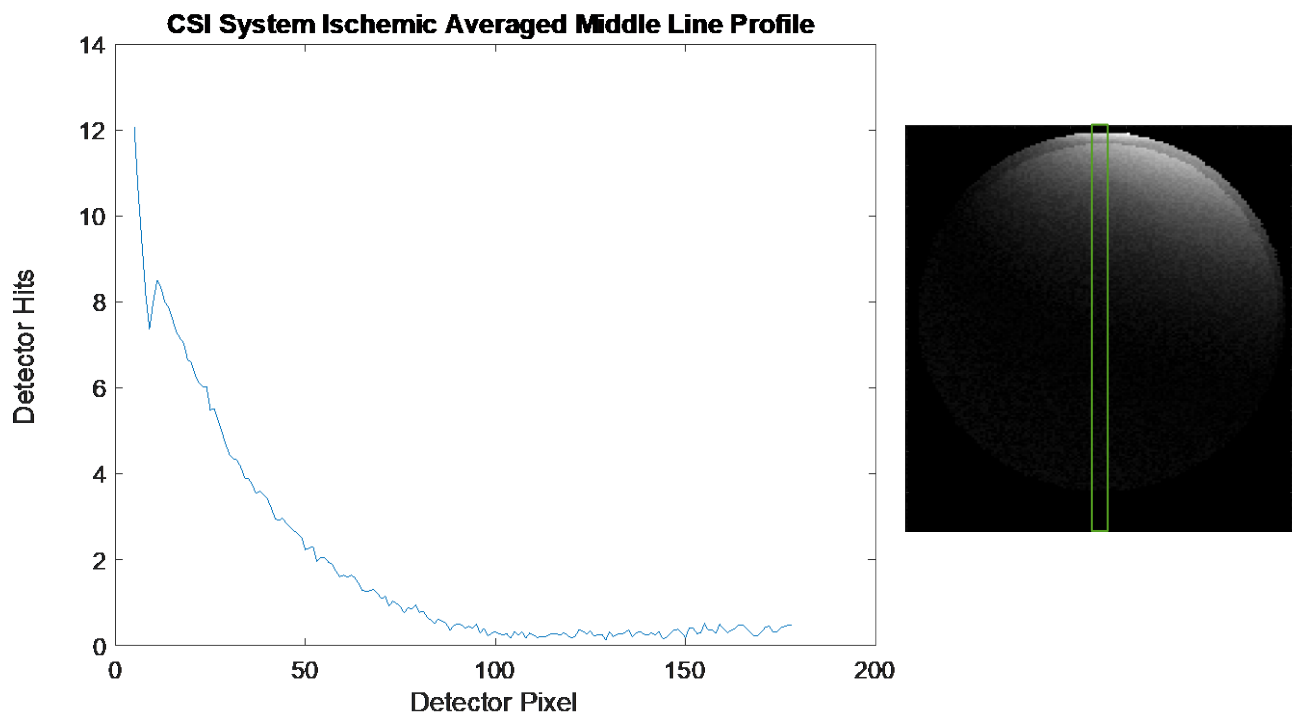
Figure 245: Line profile for attenuation.

In regard to the statistical analysis performed, a sample size of 10 images was used. The simulations were only run 10 times due to the long computational times the simulations took to perform. The computational times ranged from 91 minutes to 102 minutes. Small sample sizes in statistical analyses can affect the reliability of the results.

Chapter 10: Future Work

This research is an initial step in determining the feasibility of incorporating CSI to the Micro-X CT Scanner prototype, however, there is extensive work to be completed in the

future before the integration of CSI can be implemented. It is imperative that physical testing is completed to validate the results obtained from the Monte Carlo simulations. Physical testing is also vital to investigating the effects of limitations outlined in the results such as the use of a polychromatic tube and multiple scattering. Furthermore, simulations with stroke injured sites in difference areas of the brain should be completed. Moreover, smaller injured sites should be investigated especially since this imaging technique would be deployed within the first 4.5 hours of stroke onset, where the injured site is likely to be of a smaller size. Cadaver studies would also be helpful as obtaining phantoms with materials that produce scatter that is similar to bone and soft tissue might be hard to source.

The implementation of the edge detection algorithm with noise filters was successful in identifying the injured site boundaries. Further research and algorithm development for possible image processing techniques should be investigated. Algorithms for attenuation correction should be further researched as well as noise reduction algorithms.

Once work is completed to answer the questions formed from this study's limitations, a pre-clinical study should be completed. This would be done to investigate the medical worlds likeliness on using this as a diagnostic method.

Chapter 11: Conclusions

The proposed Compton Scatter Imaging System is not presented as a system to replace the current Micro-X CT Scanner prototype, but to be used as a secondary source of imaging information, which the diagnostic team can use to make an informed stroke diagnosis without exposing the patient to extra radiation. The aim of this project was to determine if Compton Scatter Imaging could be incorporated with the current Micro-X CT Scanner. The results from the Monte Carlo Simulations showed that ischemic tissue had a statistically significant contrast difference to healthy tissue of 2.06% (P=0.0007) while hemorrhagic tissue had a statistically significant contrast difference to healthy tissue with 4.33% (P<0.0001). It can be concluded that CSI can provide enough information to aid in the detection of strokes. Whilst this project is just preliminary work and the limitations need to be addressed in future work, the results are promising for CSI to be incorporated with the Micro-X CT Scanner.

Chapter 12: References

Agostinelli, S. *et al.* (2003) 'GEANT4 - A simulation toolkit', *Nuclear Instruments and Methods in Physics Research, Section A: Accelerators, Spectrometers, Detectors and Associated Equipment*, 506(3), pp. 250–303. doi: 10.1016/S0168-9002(03)01368-8.

AIHW (2021) *Heart, stroke and vascular disease-Australian facts*, *Australian Institute of Health and Welfare*. Available at: https://www.aihw.gov.au/reports/heart-stroke-vascular-diseases/hsvd-facts (Accessed: 2 January 2022).

Al-Bahri, J. S. and Spyrou, N. M. (1998) 'Electron density of normal and pathological breast tissues using a compton scattering technique', *Applied Radiation and Isotopes*, 49(12), pp. 1677–1684. doi: 10.1016/S0969-8043(97)10106-3.

Aronowski, J. *et al.* (2015) 'Mechanisms of Cerebral Hemorrhage', in *Stroke: Pathophysiology, Diagnosis, and Management*. Elsevier Inc., pp. 102–112. doi: 10.1016/B978-0-323-29544-4.00008-6.

Battista, J. J., Santon, L. W. and Bronskill, M. J. (1977) 'Compton scatter imaging of transverse sections: corrections for multiple scatter and attenuations', *Physics in Medicine & Biology*, 22(2), p. 229. doi: 10.1088/0031-9155/22/2/004.

Belrose, J. C. *et al.* (2012) 'Mechanisms of calcium influx following stroke', in *Metal Ion in Stroke*. Springer New York, pp. 15–39. doi: 10.1007/978-1-4419-9663-3_2.

Böhlen, T. T. *et al.* (2014) 'The FLUKA Code: Developments and Challenges for High Energy and Medical Applications', *Nuclear Data Sheets*, 120, pp. 211–214. doi: 10.1016/J.NDS.2014.07.049.

Broderick, J. P. (1997) 'Intracerebral hemorrhage after intravenous t-PA therapy for ischemic stroke', *Stroke*, 28(11), pp. 2109–2118. doi: 10.1161/01.str.28.11.2109.

Campbell, B. C. V. *et al.* (2013) 'CT perfusion improves diagnostic accuracy and confidence in acute ischaemic stroke', *Journal of Neurology, Neurosurgery and Psychiatry*, 84(6), pp. 613–618. doi: 10.1136/JNNP-2012-303752.

Carroll, K. A. L. and Chataway, J. (2006) 'Understanding stroke:Pathophysiology, presentation, and investigation', *BMJ*, 333(Suppl S3), p. 0609319. doi: 10.1136/SBMJ.0609319.

Chen, J. *et al.* (2006) 'New insights into the noise reduction Wiener filter', *IEEE Transactions on Audio, Speech and Language Processing*, 14(4), pp. 1218–1233. doi: 10.1109/TSA.2005.860851.

Demeestere, J. *et al.* (2020) 'Review of perfusion imaging in acute ischemic stroke: From time to tissue', *Stroke*, pp. 1017–1024. doi: 10.1161/STROKEAHA.119.028337.

Fassbender, K. *et al.* (2013) 'Streamlining of prehospital stroke management: the golden hour', *The Lancet. Neurology*, 12(6), pp. 585–596. doi: 10.1016/S1474-4422(13)70100-5.

Friedman, H. S. (1996) 'Tissue plasminogen activator for acute ischemic stroke.', *The New

England journal of medicine, 334(21), pp. 1405; author reply 1406. doi: 10.1056/NEJM199605233342114.

Garnett, E. S. *et al.* (1977) 'Lung density: clinical method for quantitation of pulmonary congestion and edema.', *Canadian Medical Association Journal*, 116(2), p. 153. Available at: /pmc/articles/PMC1878992/?report=abstract (Accessed: 11 January 2022).

Grotta, J. C. (2014) 'tPA for Stroke Important Progress in Achieving Faster Treatment'. doi: 10.1001/jama.2014.3203.

Del Guerra, A. *et al.* (1982) 'A Detailed Monte Carlo Study of Multiple Scattering Contamination in Compton Tomography at 90°', *IEEE Transactions on Medical Imaging*, 1(2), pp. 147–152. doi: 10.1109/TMI.1982.4307562.

Haass, A. *et al.* (2014) '"Time is brain". Optimizing prehospital stroke management', *Nervenarzt*, 85(2), pp. 189–194. doi: 10.1007/s00115-013-3952-z.

Harding, G. and Harding, E. (2010) 'Compton scatter imaging: A tool for historical exploration', *Applied Radiation and Isotopes*. Pergamon, pp. 993–1005. doi: 10.1016/j.apradiso.2010.01.035.

Harrison, R. L. (2010) 'Theoretical foundations of dynamical Monte Carlo simulations', *Data Analysis Computers in Physics*, 1204, p. 1087. doi: 10.1063/1.3295638.

Herr, M. D. *et al.* (1994) 'A Flying Spot X-Ray System for Compton Backscatter Imaging', *IEEE Transactions on Medical Imaging*, 13(3), pp. 461–469. doi: 10.1109/42.310877.

Hirayama, H and Hirayama, Hideo (2000) *Advanced Monte Carlo on Radiation Physics*.

Hubbell, J. H. *et al.* (1975) 'Atomic form factors, incoherent scattering functions, and photon scattering cross sections', *Journal of Physical and Chemical Reference Data*, 4, p. 471. doi: 10.1063/1.555523.

Hubbell, J. H., Veigele, W. J. and Briggs, E. A. (1975) 'Atomic form factors, incoherent scattering functions, and photon scattering cross sections ARTICLES YOU MAY BE INTERESTED IN', *Journal of Physical and Chemical Reference Data*, 4, p. 471. doi: 10.1063/1.555523.

Huddleston, A. L., Bhaduri, D. and Weaver, J. (1979) 'Geometrical considerations for Compton scatter densitometry', *Medical Physics*, 6(6), pp. 519–522. doi: 10.1118/1.594616.

Hui, C., Tadi, P. and Patti, L. (2021) 'Ischemic Stroke', *StatPearls*, pp. 1–14. Available at: https://www.ncbi.nlm.nih.gov/books/NBK499997/ (Accessed: 9 March 2022).

Jones, K. C. *et al.* (2018) 'Characterization of Compton-scatter imaging with an analytical simulation method', *Physics in Medicine and Biology*, 63(2), p. 25016. doi: 10.1088/1361-6560/aaa200.

Kaufman, L. *et al.* (1976) 'Measurement of absolute lung density by compton-scatter densitometry', *IEEE Transactions on Nuclear Science*, 23(1), pp. 599–605. doi: 10.1109/TNS.1976.4328313.

King, A. P. and Eckersley, R. J. (2019) 'Inferential Statistics IV: Choosing a Hypothesis Test', *Statistics for Biomedical Engineers and Scientists*, pp. 147–171. doi: 10.1016/B978-0-08-102939-8.00016-5.

Kippen, R. M. (2004) 'The GEANT low energy Compton scattering (GLECS) package for use in simulating advanced Compton telescopes', *New Astronomy Reviews*, pp. 221–225. doi: 10.1016/j.newar.2003.11.039.

Kristián, T. and Siesjö, B. K. (1998) 'Calcium in Ischemic Cell Death', *Stroke*, 29(3), pp. 705–718. doi: 10.1161/01.STR.29.3.705.

Krzywinski, M. and Altman, N. (2013) 'Points of significance: Significance, P values and t-tests', *Nature Methods*, 10(11), pp. 1041–1042. doi: 10.1038/NMETH.2698.

Kurz, K. D. *et al.* (2016) 'Radiological imaging in acute ischaemic stroke', *European Journal of Neurology*, 23, pp. 8–17. doi: 10.1111/ENE.12849.

Kwiatkowski, T. G. *et al.* (1999) 'Effects of Tissue Plasminogen Activator for Acute Ischemic Stroke at One Year', *New England Journal of Medicine*, 340(23), pp. 1781–1787. doi: 10.1056/nejm199906103402302.

Lee, J. Y. *et al.* (2012) 'The role of iron in brain following subarachnoid hemorrhage', in *Metal Ion in Stroke*. Springer New York, pp. 273–282. doi: 10.1007/978-1-4419-9663-3_13.

Lenti, M. and Veltri, M. (2011) 'Monte Carlo study of a 3D Compton imaging device with GEANT4'. doi: 10.1016/j.nima.2011.06.060.

Lin, C. M. and Selim, M. (2012) 'Iron neurotoxicity in ischemic and hemorrhagic stroke', in *Metal Ion in Stroke*. Springer New York, pp. 241–253. doi: 10.1007/978-1-4419-9663-3_11.

Lin, M. P. and Liebeskind, D. S. (2016) 'Imaging of Ischemic Stroke', *Continuum : Lifelong Learning in Neurology*, 22(5), p. 1399. doi: 10.1212/CON.0000000000000376.

Minnerup, J. *et al.* (2013) 'Stroke: Pathophysiology and Therapy', *Colloquium Series on Integrated Systems Physiology: From Molecule to Function*, 5(2), pp. 9–29. doi: 10.4199/c00088ed1v01y201308isp042.

Musuka, T. D. *et al.* (2015) 'Diagnosis and management of acute ischemic stroke: speed is critical', *CMAJ : Canadian Medical Association Journal*, 187(12), p. 887. doi: 10.1503/CMAJ.140355.

Pogson, E. M. *et al.* (2013) 'Comparing and evaluating the efficacy of the TOR18FG Leeds test X-ray phantom for T-rays.', *Quantitative Imaging in Medicine and Surgery*, 3(1), pp. 18–27. doi: 10.3978/J.ISSN.2223-4292.2013.02.05.

Queensland Brain Institue (2020) *Stroke facts* , *The University of Queensland*. Available at: https://qbi.uq.edu.au/brain/brain-diseases/stroke/stroke-facts (Accessed: 1 June 2022).

Redler, G. *et al.* (2018) 'Compton scatter imaging: A promising modality for image guidance in lung stereotactic body radiation therapy', *Medical Physics*, 45(3), pp. 1233–1240. doi: 10.1002/mp.12755.

Ryan, E. A. and Farquharson, M. J. (2007) 'Breast tissue classification using x-ray scattering measurements and multivariate data analysis', *Physics in medicine and biology*, 52(22), pp. 6679–6696. doi: 10.1088/0031-9155/52/22/009.

Ryan, E. A., Farquharson, M. J. and Flinton, D. M. (2005) 'The use of Compton scattering to differentiate between classifications of normal and diseased breast tissue', *Physics in Medicine and Biology*, 50(14), pp. 3337–3348. doi: 10.1088/0031-9155/50/14/010.

'Tissue plasminogen activator for acute ischemic stroke' (1995) *The New England journal of medicine*, 333(24), pp. 1581–1588. doi: 10.1056/NEJM199512143332401.

Wolfe, C. D. A. (2000) 'The impact of stroke', *British Medical Bulletin*, 56(2), pp. 275–286. doi: 10.1258/0007142001903120.

Yamashita, T. and Abe, K. (2020) 'Pathophysiology of Neuronal Cell Death After Stroke', in *Stroke Revisited: Pathophysiology of Stroke*. Springer, Singapore, pp. 235–241. doi: 10.1007/978-981-10-1430-7_16.

Yan, H., Tian, Z. and Shao, Y. (2018) 'Physics in Medicine & Biology Characterization of Compton-scatter imaging with an analytical simulation method Related content A new scheme for real-time high-contrast imaging in lung cancer radiotherapy: a proof-of-concept study', *Phys. Med. Biol*, 63, p. 25016. doi: 10.1088/1361-6560/aaa200.

Yang, K. *et al.* (2020) 'Quantitative evaluation of transmission properties of breast tissue equivalent materials under Compton scatter imaging setup'. doi: 10.1016/j.ejmp.2020.03.014.

Ziessman, H. A., O'Malley, J. P. and Thrall, J. H. (2006) 'Physics of Nuclear Medicine', in *Nuclear Medicine*. 3rd edn. Mosby, pp. 20–33. doi: 10.1016/B978-0-323-02946-9.50007-6.

Zou, J. *et al.* (2010) 'Geant4-based Monte Carlo simulator for fan-and cone-beam X-ray CT', *2010 4th International Conference on Bioinformatics and Biomedical Engineering, iCBBE 2010*. doi: 10.1109/ICBBE.2010.5514746.

Chapter 13: Appendices

13.1 Klein-Nishina Calculations

$\frac{d\sigma_{KN}}{d\Omega}(\theta)$ for a single electron at rest for energies 40keV – 100keV and angles 0°-180°.

Scattering Angle (°)	Incident Photon Energy (keV)						
	40	50	60	70	80	90	100
0	1	1	1	1	1	1	1
15	0.9615	0.96	0.959	0.9575	0.9565	0.955	0.954
30	0.857	0.8525	0.848	0.844	0.8395	0.8355	0.831
45	0.717	0.709	0.7015	0.694	0.6865	0.6795	0.6725
60	0.5795	0.569	0.559	0.5495	0.54	0.531	0.522
75	0.478	0.4659	0.4545	0.4435	0.433	0.4235	0.414
90	0.4325	0.41845	0.412	0.393	0.3815	0.371	0.361
105	0.4455	0.4285	0.4055	0.3975	0.3835	0.371	0.359
120	0.5055	0.4825	0.4615	0.442	0.4245	0.4085	0.3935
135	0.5895	0.5595	0.532	0.507	0.4845	0.464	0.445
150	0.6735	0.6355	0.602	0.5715	0.544	0.5185	0.4955
165	0.7335	0.6905	0.6525	0.6175	0.5865	0.558	0.532
180	0.7555	0.7105	0.6705	0.6345	0.6015	0.572	0.545

13.2 Calculations of x in S(x,Z)

E (keV)	40	50	60	70	80	90	100
λ	0.309963	0.2479704	0.206642	0.17712171	0.1549815	0.13776133	0.1239852

q(°)	sin(θ/2)	sin (θ/2)/ λ						
15	0.13052619	0.42110249	0.52637812	0.63165374	0.73692936	0.84220499	0.94748061	1.05275623
30	0.25881905	0.83499981	1.04374976	1.25249971	1.46124966	1.66999961	1.87874957	2.08749952
45	0.38268343	1.23461004	1.54326255	1.85191506	2.16056757	2.46922008	2.77787259	3.0865251
60	0.5	1.61309576	2.0163697	2.41964363	2.82291757	3.22619151	3.62946545	4.03273939
75	0.60876143	1.96398096	2.45497619	2.94597143	3.43696667	3.92796191	4.41895715	4.90995239
90	0.70710678	2.2812619	2.85157737	3.42189284	3.99220832	4.56252379	5.13283927	5.70315474
105	0.79335334	2.55950981	3.19938727	3.83926472	4.47914217	5.11901963	5.75889708	6.39877453
120	0.8660254	2.79396381	3.49245476	4.19094571	4.88943666	5.58792762	6.28641857	6.98490952
135	0.92387953	2.98061231	3.72576538	4.47091846	5.21607154	5.96122461	6.70637769	7.45153077
150	0.96592583	3.1162617	3.89532713	4.67439255	5.45345798	6.23252341	7.01158883	7.79065426
165	0.99144486	3.198591	3.99823875	4.7978865	5.59753425	6.397182	7.19682974	7.99647749
180	1	3.22619151	4.03273939	4.83928727	5.64583515	6.45238303	7.2589309	8.06547878

13.3 Incoherent Scatter Function

13.3.1 40keV

Angle	H	C	O	Ca	Fe
15	0.98298	0.69728333	0.657125	0.4895	0.41280769
30	0.9977	0.84185	0.8245	0.68175	0.64734615
45	0.9999	0.93588333	0.9019875	0.8019	0.76765385
60	1	0.96343333	0.93275	0.84605	0.81142308
75	1	0.98836667	0.970525	0.8985	0.87323077
90	1	0.9925	0.975	0.91	0.88461538
105	1	0.99616667	0.9874875	0.92655	0.90961538

120	1	0.998	0.990375	0.935	0.91923077
135	1	0.99861667	0.994625	0.943	0.93138462
150	1	0.99861667	0.994625	0.945	0.93138462
165	1	0.99861667	0.994625	0.9453	0.93253846
180	1	0.99946667	0.9975875	0.9455	0.93961538

13.3.2 50keV

Angle	H	C	O	Ca	Fe
15	0.9502	0.74628333	0.7285	0.5785	0.48796154
30	0.9995	0.89141667	0.862625	0.7415	0.71107692
45	1	0.96343333	0.93275	0.84605	0.81142308
60	1	0.98836667	0.970525	0.8985	0.87323077
75	1	0.99616667	0.9874875	0.92655	0.90961538
90	1	0.99666667	0.99	0.93655	0.88461538
105	1	0.9985	0.994625	0.9453	0.93138462
120	1	0.99946667	0.9975875	0.95955	0.94607692
135	1	0.9995	0.998125	0.96275	0.95
150	1	0.99966667	0.998875	0.9695	0.95192308
165	1	0.99966667	0.998875	0.97	0.95384615
180	1	0.99966667	0.998875	0.97055	0.95719231

13.3.3 60keV

Angle	H	C	O	Ca	Fe
15	0.99837	0.78171667	0.771875	0.60815	0.55165385
30	0.99999	0.93588333	0.9019875	0.8019	0.76765385

45	1	0.98836667	0.9705375	0.8985	0.87323077
60	1	0.99616667	0.987375	0.92655	0.90961538
75	1	0.99861667	0.994625	0.9453	0.93138462
90	1	0.99946667	0.9975875	0.95955	0.94607692
105	1	0.9995	0.998875	0.97055	0.95719231
120	1	0.9995	0.998875	0.97055	0.95719231
135	1	0.9995	0.9995	0.976	0.96111538
150	1	0.99966667	0.999625	0.9785	0.96923077
165	1	0.99966667	0.99975	0.98	0.97115385
180	1	0.99983333	0.9998625	0.9815	0.97269231

13.3.4 70keV

Angle	H	C	O	Ca	Fe
15	0.9941	0.81296667	0.801375	0.64765	0.60446154
30	1	0.96343333	0.93275	0.84605	0.81142308
45	1	0.98836667	0.9705	0.8985	0.87323077
60	1	0.99861667	0.994625	0.9453	0.93138462
75	1	0.99946667	0.9975875	0.95955	0.94607692
90	1	0.99976667	0.998875	0.97055	0.95719231
105	1	0.99983333	0.99925	0.97795	0.96496154
120	1	0.99983333	0.9995875	0.9835	0.97115385
135	1	0.99995	0.9997375	0.9855	0.97615385
150	1	0.99996667	0.9998625	0.9865	0.97884615
165	1	0.99996667	0.999875	0.9875	0.98038462

Angle	H	C	O	Ca	Fe
180	1	0.99998333	0.999875	0.9895	0.98192308

13.3.5 80keV

Angle	H	C	O	Ca	Fe
15	0.9977	0.84185	0.8245	0.68175	0.64734615
30	1	0.96343333	0.93275	0.84605	0.81142308
45	1	0.99616667	0.9874875	0.92655	0.90961538
60	1	0.99861667	0.994625	0.9453	0.93138462
75	1	0.99976667	0.998875	0.97055	0.95719231
90	1	0.99976667	0.99925	0.9778	0.96546154
105	1	0.99995	0.9997125	0.9849	0.98196154
120	1	0.99996667	0.99985	0.9875	0.97653846
135	1	0.99998333	0.9999125	0.99245	0.98403846
150	1	1	0.999925	0.99265	0.98423077
165	1	1	0.9999375	0.99345	0.98730769
180	1	1	0.99995	0.9945	0.99153846

13.3.6 90keV

Angle	H	C	O	Ca	Fe
15	0.9999	0.86808333	0.844375	0.7128	0.68219231
30	1	0.98836667	0.970525	0.8985	0.87323077
45	1	0.99861667	0.994625	0.92655	0.90961538
60	1	0.99946667	0.9975875	0.95955	0.94607692
75	1	0.99981667	0.99925	0.9778	0.96546154
90	1	0.99995	0.9997125	0.9849	0.97346154

105	1	0.99996667	0.99985	0.9875	0.97653846
120	1	1	0.9999125	0.99245	0.98403846
135	1	1	0.99995	0.9975	0.98615385
150	1	1	0.999975	0.99962	0.99057692
165	1	1	0.9999875	0.999645	0.99076923
180	1	1	1	0.99967	0.99111538

13.3.7 100keV

Angle	H	C	O	Ca	Fe
15	0.98298	0.89141667	0.862625	0.7415	0.71107692
30	0.9977	0.98836667	0.970525	0.8985	0.87323077
45	0.9999	0.99861667	0.994625	0.9453	0.93138462
60	1	0.99976667	0.998875	0.97055	0.95719231
75	1	0.9995	0.9997125	0.9849	0.97346154
90	1	0.99998333	0.9999125	0.99045	0.98403846
105	1	1	0.9999875	0.99395	0.98403846
120	1	1	0.9999875	0.9962	0.99057692
135	1	1	1	0.99705	0.99211538
150	1	1	1	0.99755	0.99307692
165	1	1	1	0.99805	0.99407692
180	1	1	1	0.99805	0.99446154

13.4 Atom-Bound Klein-Nishina Scatter Cross-sections for Hydrogen, Carbon, Oxygen, Calcium and Iron

13.4.1 40keV

Angle (°)	Scatter Cross-sections				
	H	C	O	Ca	Fe
15	0.94513527	0.67043793	0.63182569	0.47065425	0.3969146
30	0.8550289	0.72146545	0.7065965	0.58425975	0.55477565
45	0.7169283	0.67102835	0.64672504	0.5749623	0.55040781
60	0.5795	0.55830962	0.54052863	0.49028598	0.47021967
75	0.478	0.47243927	0.46391095	0.429483	0.41740431
90	0.4325	0.42925625	0.4216875	0.393575	0.38259615
105	0.4455	0.44379225	0.43992568	0.41277803	0.40523365
120	0.5055	0.504489	0.50063456	0.4726425	0.46467115
135	0.5895	0.58868453	0.58633144	0.5558985	0.54905123
150	0.6735	0.67256833	0.66987994	0.6364575	0.62728754
165	0.7335	0.73248533	0.72955744	0.69337755	0.68401696
180	0.7555	0.75509707	0.75367736	0.71432525	0.70987942

$$\frac{d\sigma_{KN}(\theta)}{d\Omega} \; (r_e^2)$$
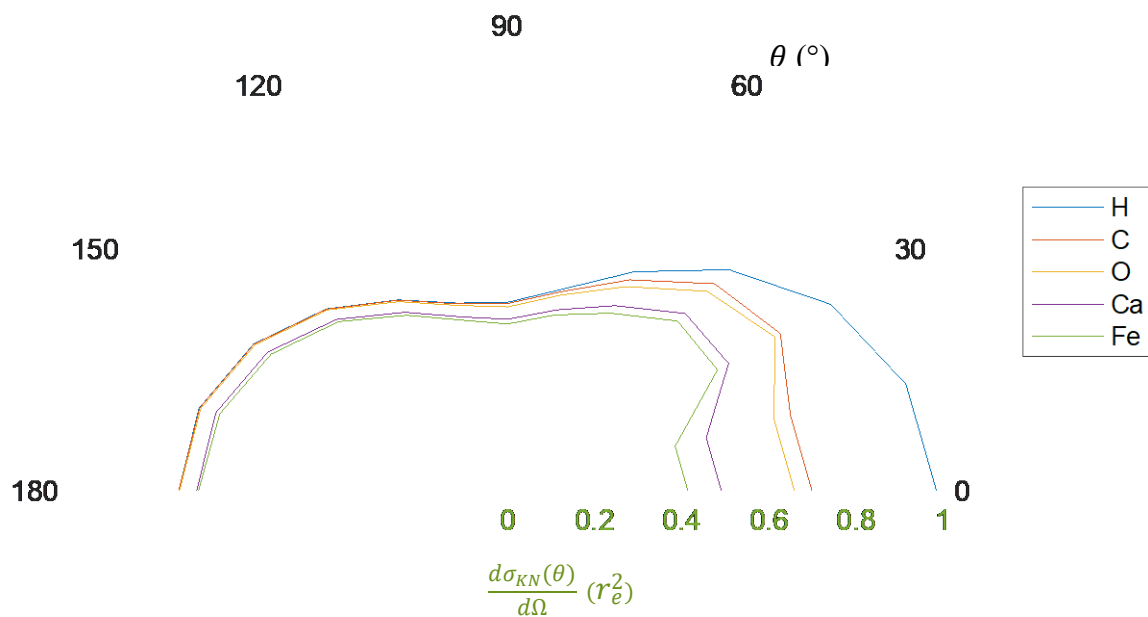
13.4.2 50keV

Angle (°)	Scatter Cross-sections				
	H	**C**	**O**	**Ca**	**Fe**
15	0.912192	0.716432	0.69936	0.55536	0.46844308
30	0.85207375	0.75993271	0.73538781	0.63212875	0.60619308
45	0.709	0.68307423	0.66131975	0.59984945	0.57529896
60	0.569	0.56238063	0.55222873	0.5112465	0.49686831
75	0.4659	0.46411405	0.46007043	0.43167965	0.42378981
90	0.41845	0.41705517	0.4142655	0.39189935	0.37016731
105	0.4285	0.42785725	0.42619681	0.40506105	0.39909831
120	0.4825	0.48224267	0.48133597	0.46298288	0.45648212
135	0.5595	0.55922025	0.55845094	0.53865863	0.531525
150	0.6355	0.63528817	0.63478506	0.61611725	0.60494712

165	0.6905	0.69026983	0.68972319	0.669785	0.65863077
180	0.7105	0.71026317	0.70970069	0.68957578	0.68008513

$$\frac{d\sigma_{KN}(\theta)}{d\Omega}\ (r_e^2)$$
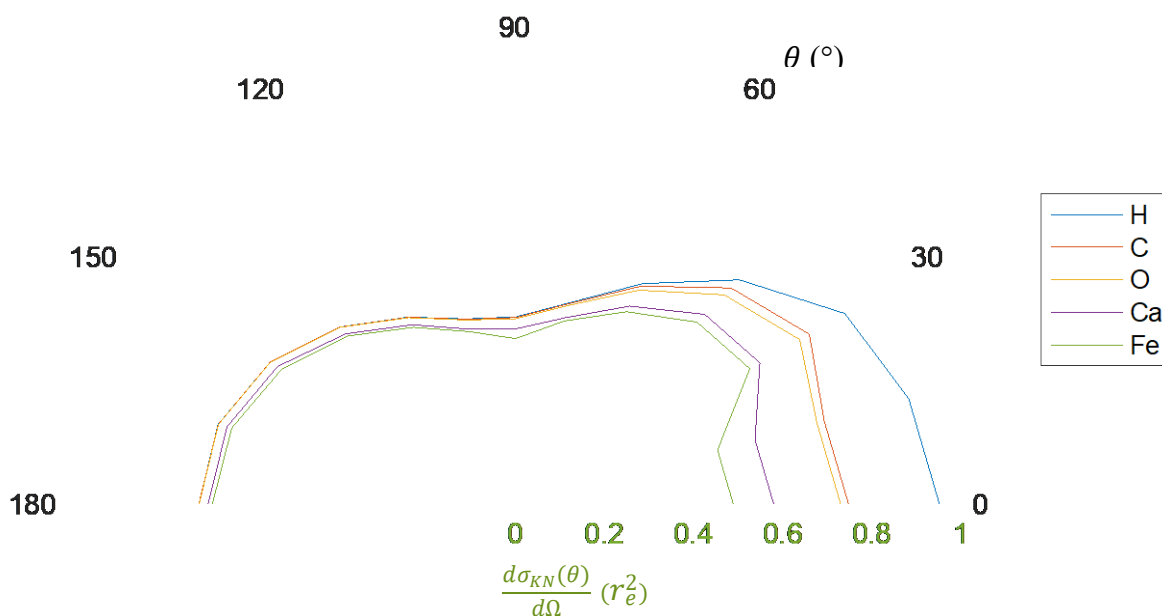
13.4.3 60keV

Angle (°)	Scatter Cross-sections				
	H	C	O	Ca	Fe
15	0.95743683	0.74966628	0.74022813	0.58321585	0.52903604
30	0.84799152	0.79362907	0.7648854	0.6800112	0.65097046
45	0.7015	0.69333922	0.68083206	0.63029775	0.61257138
60	0.559	0.55685717	0.55194263	0.51794145	0.508475
75	0.4545	0.45387128	0.45205706	0.42963885	0.42331431
90	0.412	0.41178027	0.41100605	0.3953346	0.38978369
105	0.4055	0.40529725	0.40504381	0.39355803	0.38814148

120	0.4615	0.46126925	0.46098081	0.44790883	0.44174425
135	0.532	0.531734	0.531734	0.519232	0.51131338
150	0.602	0.60179933	0.60177425	0.589057	0.58347692
165	0.6525	0.6522825	0.65233688	0.63945	0.63367788
180	0.6705	0.67038825	0.67040781	0.65809575	0.65219019
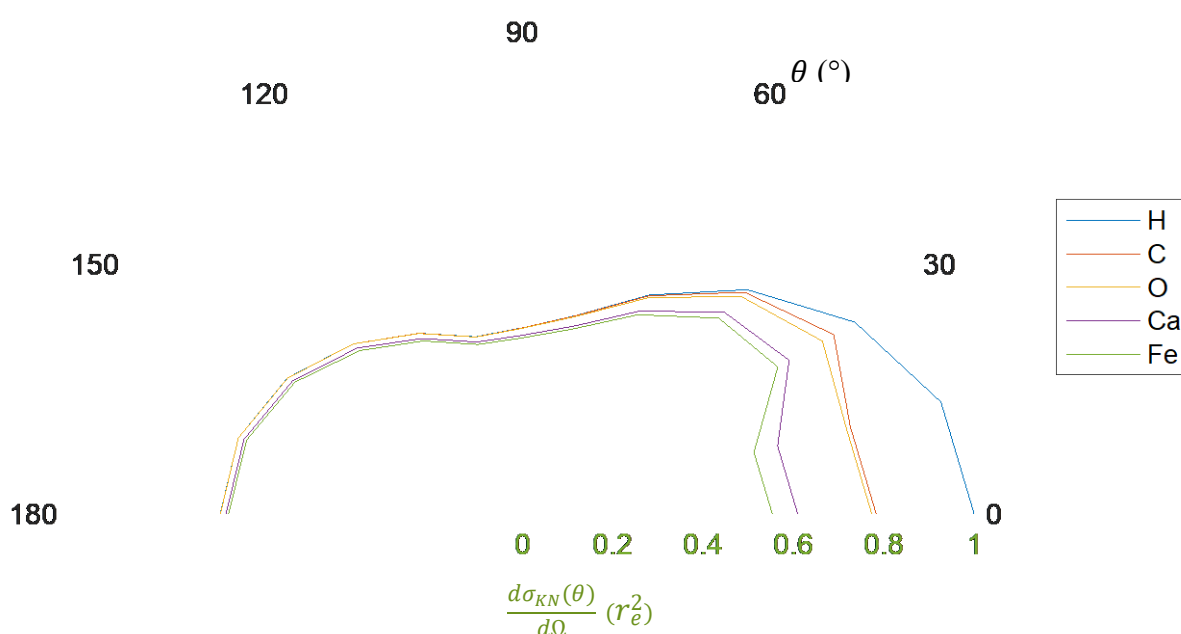
13.4.4 70keV

Angle (°)	Scatter Cross-sections				
	H	C	O	Ca	Fe
15	0.95185075	0.77841558	0.76731656	0.62012488	0.57877192
30	0.844	0.81313773	0.787241	0.7140662	0.68484108
45	0.694	0.68592647	0.673527	0.623559	0.60602215

60	0.5495	0.54873986	0.54654644	0.51944235	0.51179585
75	0.4435	0.44326347	0.44243006	0.42556043	0.41958512
90	0.393	0.3929083	0.39255788	0.38142615	0.37617658
105	0.3975	0.39743375	0.39720188	0.38873513	0.38357221
120	0.442	0.44192633	0.44181768	0.434707	0.42925
135	0.507	0.50697465	0.50686691	0.4996485	0.49491
150	0.5715	0.57148095	0.57142142	0.56378475	0.55941058
165	0.6175	0.61747942	0.61742281	0.60978125	0.6053875
180	0.6345	0.63448943	0.63442069	0.62783775	0.62303019

$\frac{d\sigma_{KN}(\theta)}{d\Omega}\ (r_e^2)$
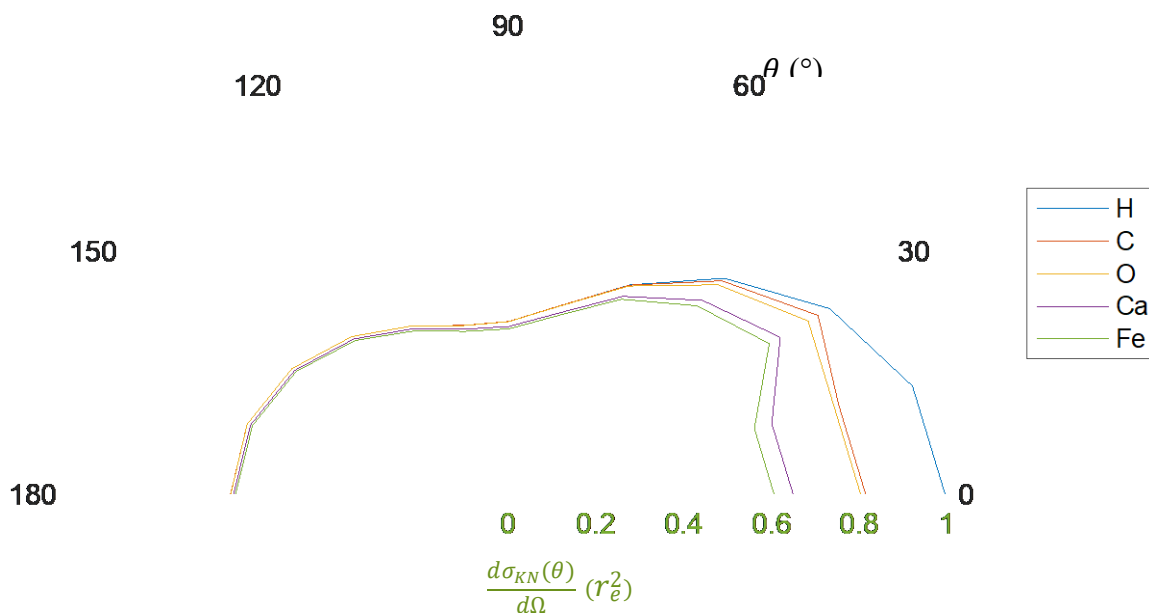
13.4.5 80keV

Scatter Cross-sections

Angle (°)	H	C	O	Ca	Fe
15	0.95430005	0.80522953	0.78863425	0.65209388	0.6191866
30	0.8395	0.80880228	0.78304363	0.71025898	0.68118967
45	0.6865	0.68386842	0.67791017	0.63607658	0.62445096
60	0.54	0.539253	0.5370975	0.510462	0.50294769
75	0.433	0.43289897	0.43251288	0.42024815	0.41446427
90	0.3815	0.38141098	0.38121388	0.3730307	0.36832358
105	0.3835	0.38348083	0.38338974	0.37770915	0.37658225
120	0.4245	0.42448585	0.42443633	0.41919375	0.41454058
135	0.4845	0.48449193	0.48445761	0.48084203	0.47676663
150	0.544	0.544	0.5439592	0.5400016	0.53542154
165	0.5865	0.5865	0.58646334	0.58265843	0.57905596
180	0.6015	0.6015	0.60146993	0.59819175	0.59641038

90

120

60 θ (°)

150

30

	H
	C
	O
	Ca
	Fe

180

0

0   0.2   0.4   0.6   0.8   1

$$\frac{d\sigma_{KN}(\theta)}{d\Omega}\ (r_e^2)$$
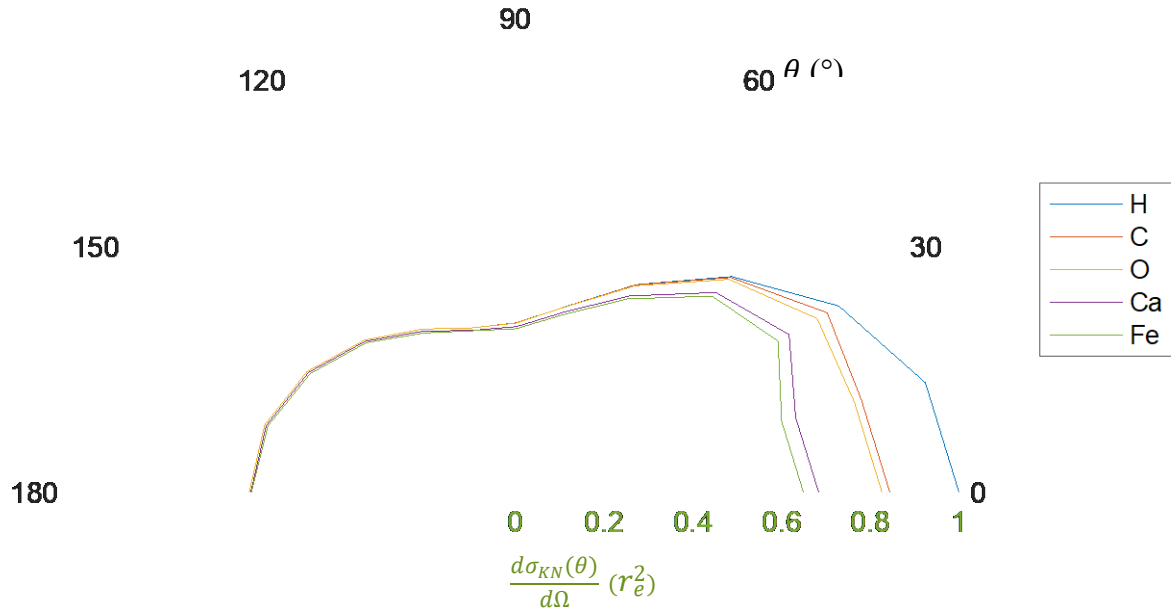
13.4.6 90keV

	Scatter Cross-sections				
Angle (°)	**H**	**C**	**O**	**Ca**	**Fe**
15	0.9549045	0.82901958	0.80637813	0.680724	0.65149365
30	0.8355	0.82578035	0.81087364	0.75069675	0.72958431
45	0.6795	0.67856003	0.67584769	0.62959073	0.61808365
60	0.531	0.5307168	0.52971896	0.50952105	0.50236685
75	0.4235	0.42342236	0.42318238	0.4140983	0.40887296
90	0.371	0.37098145	0.37089334	0.3653979	0.36115423
105	0.371	0.37098763	0.37094435	0.3663625	0.36229577
120	0.4085	0.4085	0.40846426	0.40541583	0.40197971
135	0.464	0.464	0.4639768	0.46284	0.45757538
150	0.5185	0.5185	0.51848704	0.51830297	0.51361413

165	0.558	0.558	0.55799303	0.55780191	0.55284923
180	0.572	0.572	0.572	0.57181124	0.566918

$$\frac{d\sigma_{KN}(\theta)}{d\Omega}\ (r_e^2)$$
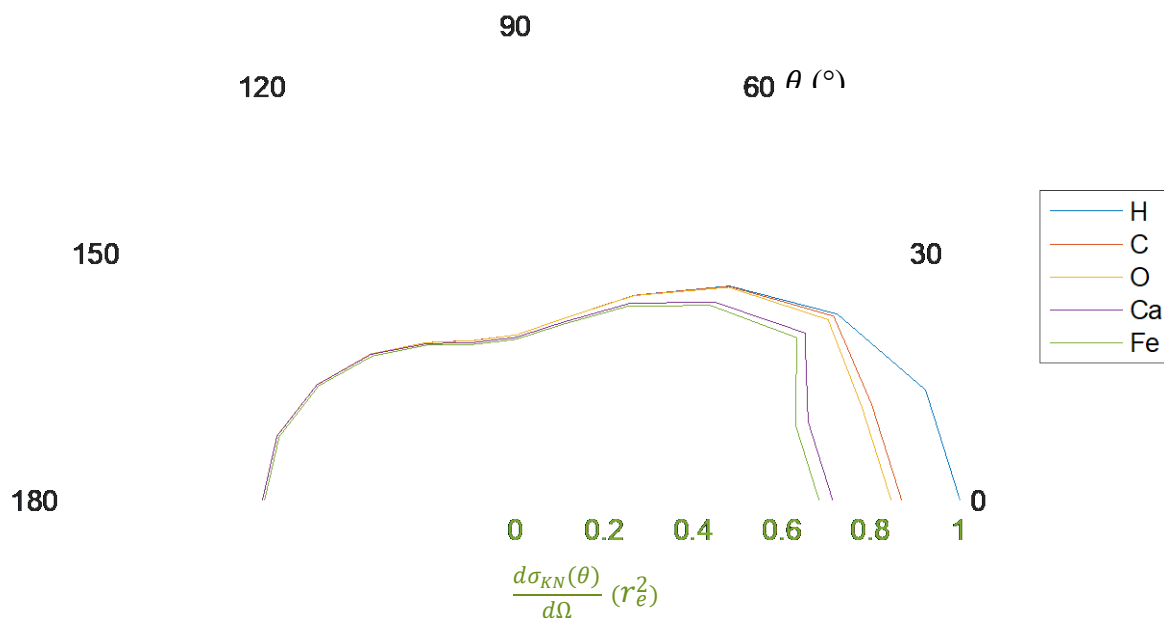
13.4.7 100keV

	Scatter Cross-sections				
Angle (°)	H	C	O	Ca	Fe
15	0.93776292	0.8504115	0.82294425	0.707391	0.67836738
30	0.8290887	0.8213327	0.80650628	0.7466535	0.72565477
45	0.67243275	0.67156971	0.66888531	0.63571425	0.62635615
60	0.522	0.5218782	0.52141275	0.5066271	0.49965438
75	0.414	0.413793	0.41388098	0.4077486	0.40301308
90	0.361	0.36099398	0.36096841	0.35755245	0.35523788
105	0.359	0.359	0.35899551	0.35682805	0.35326981

120	0.3935	0.3935	0.39349508	0.3920047	0.38979202
135	0.445	0.445	0.445	0.44368725	0.44149135
150	0.4955	0.4955	0.4955	0.49428603	0.49206962
165	0.532	0.532	0.532	0.5309626	0.52884892
180	0.545	0.545	0.545	0.54393725	0.54198154
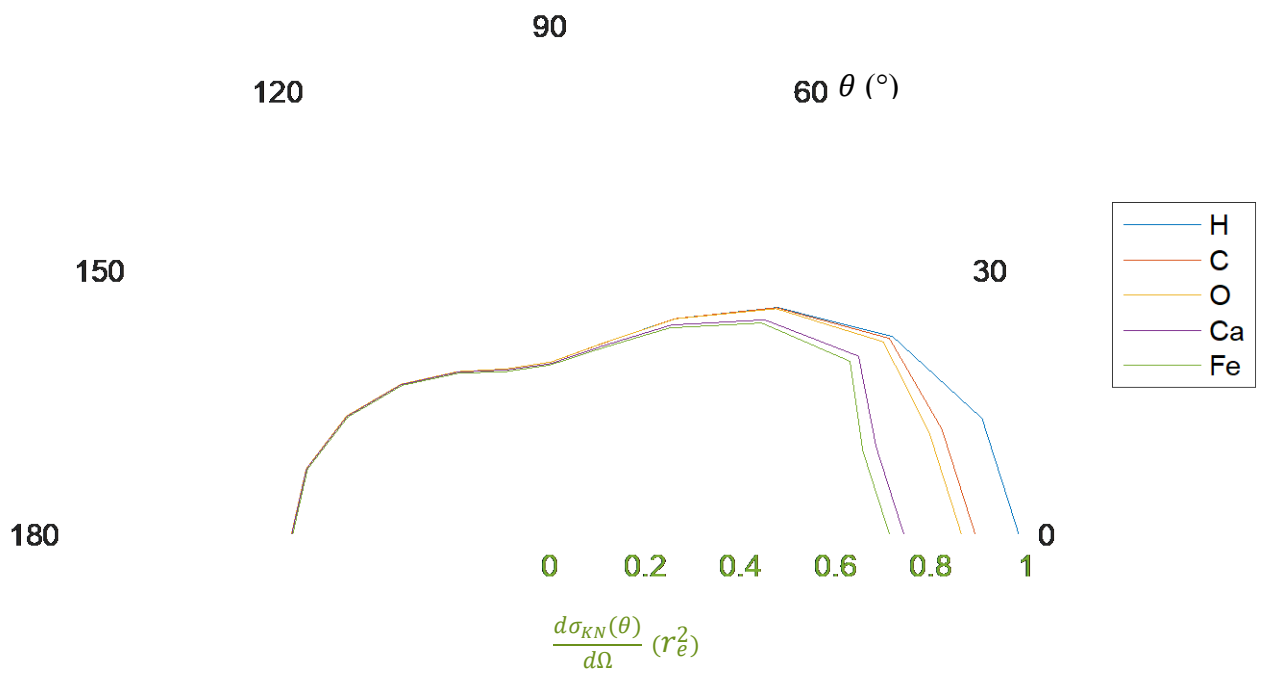
13.5 Phantom dimensions

y	Y (cm)	X(cm)
A (skull)	17.48	13.11
B (brain)	16.61	12.58

C (injury)	5.89	2.09
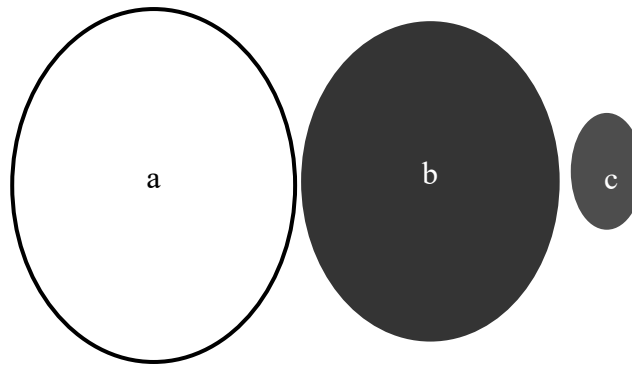
13.6 Percentage Difference

Angle	$d\Omega_H$	$d\Omega_S$	$\dfrac{|d\Omega_H - d\Omega_S|}{\dfrac{d\Omega_H + d\Omega_S}{2}}$
120	0.50354119	0.4776425	5.23
135	0.58817199	0.5573985	5.37
150	0.67198276	0.6364575	**5.43**
165	0.73184759	0.69337755	5.39